Universidad Pública de Navarra
Nafarroako Unibertsitate Publikoa

MASTER THESIS

POSTGRADUATE PROGRAM: COMMUNICATIONS

METAMATERIALS FOR ENHANCED LIGHT CONTROL:
FROM HIGH RESOLUTION FOCUSING TO INVISIBILITY

Presented by: Bakhtiyar Orazbayev.

Director: Dr. Miguel Beruete Díaz

Pamplona, July 2015

Acknowledgments

I would like to take this chance to extend my gratitude to all people who helped me during my study. The master thesis would not be accomplished without their help. However, it is not possible to include all of them in this short acknowledgement. Hope those people I missed out in the following can accept my sincere appreciation at this moment.

At first, I would like to express my gratitude to my supervisor Dr. Miguel Beruete for his excellent guidance (not just scientific). His advice and encouragement have been of vital importance during my research work. I also would like to thank Dr. Miguel Navarro-Cía for his constant support during my study. Thanks then goes to Dr. Andrea Alù. The valuable discussions with him, his advices, and experienced instruction helped greatly with my research work. I want to give my special thanks to Prof. Mario Sorolla, who unfortunately passed away. Without him it would have been impossible to make this work. In the Department of Electronic and Electrical Engineering, there are still more people I want to thank.

During my study in Spain, I am lucky to have the company of my friends and colleagues: Unai Beaskotxea, Víctor Pacheco-Peña, Pablo Rodriguez and Dr. Víctor Torres, who helped me in solving my doubts.

I acknowledge Spanish Ministerio de Economía y Competitividad for the financial support (under grant FPI BES-2012-054909) of my study at UPNA.

Last, but of course not least, I thank my parents for their love and support all the time.

Abstract

Artificial dielectrics and their descendants – metamaterials, have unusual electromagnetic parameters and provide more abilities than naturally available dielectrics for control of the light. The first experimental realization of a double negative medium gave an enormous impulse for research in the field of electromagnetism. As result, a lot of fascinating electromagnetic devices have been developed since then, including metamaterial lenses, beam steerers and even invisibility cloaks. The aim of this master thesis is to contribute to the development of such devices, especially metamaterial lenses and invisibility cloaks.

First, a background of metamaterial and metasurfaces is introduced. The main aspects of metamaterials and their characteristics are reviewed, so that the working principles of metamaterials can be acquired with minimal prerequisite mathematics. Then we review the design process of several metamaterial lenses, including a zoned fishnet metamaterial lens and a Soret lens, a member of Fresnel zone plate lenses. Finally we design a carpet cloak, using a metasurface with double ring resonators.

In the first application, the time-honored zoning technique is used to reduce the volume, and therefore weight, of a fishnet metamaterial lens. By properly optimizing a profile of the zoned lens we are able to reduce a volume of the lens up to 60% and broaden the fractional bandwidth up to 3 times. With this optimization technique the bandwidth of the zoned lens, which usually is narrow band, increases without causing any deterioration in its performance.

The second metamaterial lens is a member of the well-known Fresnel zone plate's family and consists of alternating and opaque concentric rings. Since half of the power is blocked by opaque rings the efficiency of such lenses is low. In order to improve the coupling and illumination efficiency we propose using an array of subwavelength holes instead of the transparent ring. Also by supporting the lens with a block of fishnet metamaterial working in near-zero index regime it is possible to improve radiation characteristics of a metalens antenna, such as directivity and side lobe level.

Finally, in the third application a ground cloak design is described as simulation results. The presented ground cloak is based on a metasurface, an array of closed ring resonators, and, therefore, has an ultrathin design and relatively simple in fabrication. The proposed cloak has been successfully employed to conceal an electrically large object ($1.1\lambda_0$) for wide range of incident angles and relatively wide frequency range.

Table of Contents

1 Chapter I. Introduction

Control of the light has been one of most important quests in the field of electromagnetism. Since late '40s of 20th century, when the first artificial dielectrics were proposed [1], [2], many researchers have been investigating the electromagnetic properties of such materials and their possible applications. The great interest to this man-made materials can be explained by the fact that a permittivity (and also a permeability in case of their successors – metamaterials) can be tailored at will, including values of permittivity less than unity and even negative, which is unattainable with conventional dielectrics, commonly used in microwaves and optics [3], [4]. More recently, with the appearance of metasurfaces, which are successors of frequency selective surfaces (FSS) and consist of a monolayer of photonic artificial atoms, many attractive functionalities have been also offered for shaping wave fronts of light by introducing an abrupt interfacial phase discontinuity.

Both metamaterial and metasurface give a fascinating possibility of control over electromagnetic wave propagation, which results in many interesting concepts and real applications, such as perfect lens [5], chiral lens [6], super lens [7], hyper lens [8], invisibility cloaks [9], [10], beam steerers [11] to name a few.

This chapter is divided in two sections: in the first section, the definition and main features of metamaterials and metasurfaces are presented. The attention is centered in the fishnet metamaterial and a metasurface based on closed ring resonators (CRR), which will be used in subsequent chapters. The second section describes how this Master Thesis is organized.

1.1 Background on Metamaterials and Metasurfaces.

The term metamaterials originates from Greek word “meta” (which means beyond) and refers to materials with electromagnetic parameters that are not available in the conventional materials, materials that cannot be found in the nature [3], [4]. The precursors of metamaterials are the well-known artificial dielectrics [1], [2]. These materials trace back to the 1940s and were principally used for antennas applications. In his seminal paper [12] Kock demonstrated a metal-lens antenna with the ability to focus electromagnetic waves using conducting plates. The refractive index in this metal-lens antenna could be less than unity, which changes the lens profile from convex to concave and provides new possibilities for lens design.

Later, Veselago proposed the possibility of negative-index materials[13], i.e. materials with simultaneous negative permittivity and permeability values ($\varepsilon, \mu < 0$). He predicted that such media has negative index of refraction and that some laws are reversed: Snell’s law, Doppler effect and Cerenkov effect. The media proposed by Veselago were considered unrealizable due to the difficulty to get an effective negative permeability. This changed in 1999, when Pendry proposed a nonmagnetic particle with a strong magnetic response[14], The particle proposed by Pendry was a split-ring resonator (SRR) and had dimensions smaller than the wavelength. Thanks to its strong magnetic response, the particle exhibits a negative effective permeability value, i.e.,

the metamaterial, which is built using this particle, can be considered as a negative permeability material (MNG). Based on this work, Smith in 2000 demonstrated a double negative material (DNG) [15], [16]. It consisted of SRRs overlapping with a medium with effective negative electric permittivity, so that negative values of permeability and permittivity were synthesized simultaneously. The medium with negative refractive index was experimentally demonstrated in 2001 by Shelby[17], which gave a great impulse to metamaterials research.

There are basically four different classes of materials[18], [19]: a) double positive (DPS) or right-handed media (RHM), b) double negative (DNG) or left-handed media (LHM), c) negative permeability (MNG) media and d) negative permittivity (ENG) media. A general classification of materials is presented in Fig. 1.1, where μ and ε used as y and x axis respectively [19].

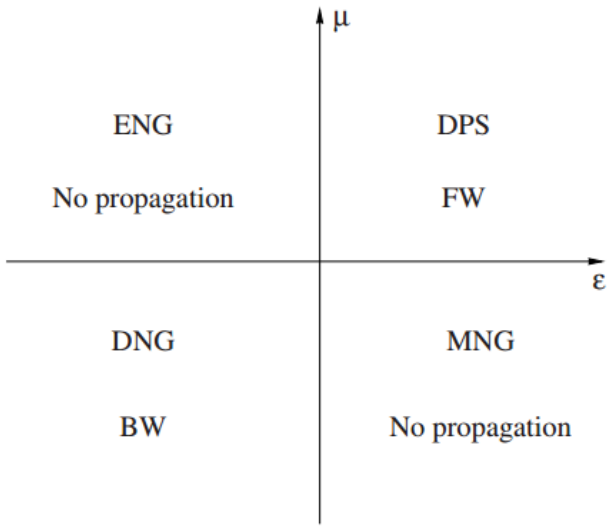

Fig. 1.1. Classification of materials in the in the ε, μ plane. ©2007 JCTE,[19]. First quarter – doubly positive (DPS) materials (ε, μ > 0) with forward (FW) propagating waves; second quarter – materials with negative permittivity (ENG), (ε < 0) and no propagation; third quarter – doubly negative (DNG) materials (ε, μ < 0) with backward propagation; fourth quarter – materials with negative permeability (MNG), (μ < 0) and no propagation.

1.1.1 Fishnet metamaterial

Metamaterials based on SRR usually suffer from increasing losses as the frequency increases and therefore their use is limited at microwaves. From this point of view, one of the most promising metamaterials with effective negative refractive index (NRI) at millimeter waves and visible wavelengths[20] is a fishnet metamaterial, see Fig.1.2. Several works have confirmed that the general underlying physics of the fishnet metamaterial relies primarily on complex surface waves[21], [22]. This mechanism provides NRI and has considerably low losses at millimeter waves and terahertz range[23]–[27]. In addition, the complex surface waves mechanism could increase the coupling-in and –out, guaranteeing a good impedance matching[28], and may

improve the effective illumination and extend radiating area[29]. Another mechanism responsible for low losses in fishnet metamaterial is the extraordinary optical transmission phenomena (EOT), which takes place in stacked subwavelength hole arrays (SSHA)[24], [30].

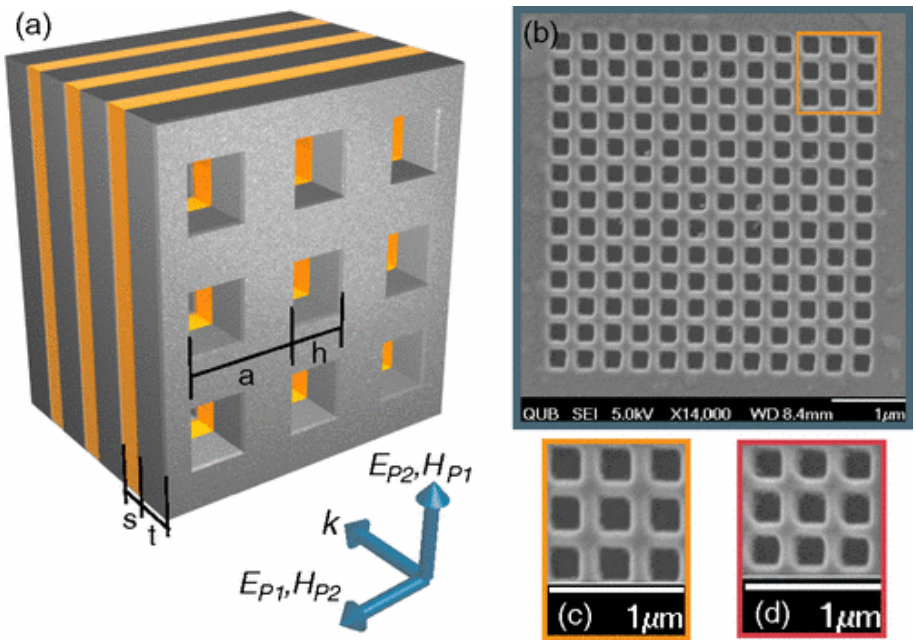

Fig.1.2. Schematic of a fishnet metamaterial. ©2011 APS,[20].

An interesting feature of the fishnet metamaterial and metamaterials in general, that enables independent control of the permittivity ε and permeability μ at will, is that they can be ideally matched with free space when the normalized characteristic impedance $\eta = (\mu/\varepsilon)^{1/2} = 1$, for example, when both permittivity and permeability are equal to -1.

The intensive research on metamaterials and their applications paid off in a huge amount of publications, including investigations of fishnet metamaterial. The *Antennas Group-TERALAB* made contribution to this field by writing more than 30 publications, including research on metamaterial lenses. Among them are works on fishnet metamaterial lenses and zoned fishnet metamaterial lenses. It was demonstrated, that fishnet metamaterial, due to its lower losses and frequency-robust magnetic response at frequencies higher than microwave[31], can be successfully applied in metamaterial lenses, improving the impedance matching without the need of additional anti-reflection coatings[32]–[34]. Subsequently, it was proposed to apply the time-honored zoning technique, in order to reduce thickness and, therefore weight and losses[35]–[37].

In this Master Thesis we continue work on zoned fishnet metamaterial lenses and propose a smart optimization procedure to broaden the usually narrow bandwidth of the zoned lens. A secret ingredient of this technique is the highly dispersive nature of the fishnet metamaterial, which allows to have more than one optimal zoned lens profile for different frequencies. The details of this procedure will be described in Chapter III. Getting ahead we can say that the fabricated lens demonstrates a good performance and even outperforms silicon zoned lens, commonly used in microwave range, in terms of impedance matching.

However, the fishnet metamaterial can be used not only in lens with traditional non-zoned or zoned lens profile but also for Fresnel zone plate lenses. The leaky wave mechanism of the fishnet metamaterial could improve here the effective illumination and extend the radiating area[29], making possible to build a compact Fresnel zone plate antenna with small focus/diameter ratio[38]. This will be described in detail also in Chapter III.

1.1.2 Metasurface based on closed ring resonators (CRR)

Recently, an evolution of metamaterials – metasurfaces, which consist of only a monolayer of planar metallic structures, have shown great potential for achieving full control of the wave front of light , with low fabrication cost as they do not require complicated three-dimensional (3D) nanofabrication techniques. Metasurfaces, having their roots in frequency selective surfaces (FSS), are able to generate an abrupt interfacial phase changes, which gives a possibility of controlling the local wave front at the subwavelength scale[39], [40]. A high variety of applications based on metasurfaces have been proposed and demonstrated, such as wave plates[39], [41], ultrathin metalenses[42], [43], quarter-wave plates[44] and many others.

In this thesis we use a particular metasurface design, which consists of an array of CRR, see Fig.1.3. The control of local phase response is realized by changing the radii of each element. By this, we change the surface impedance of the unit cells and therefore the phase of the reflected wave.

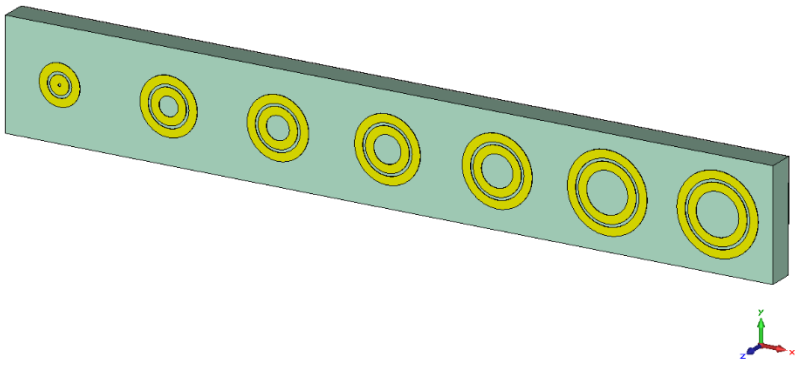

Fig.1.3. Metasurface based on array of closed ring resonators.

We use such metasurface to create a specified phase distribution on the edge of the object, which we want to hide from the incident wave and is placed on the ground plane. This phase is determined by the height of the object and should compensate the difference between incident and reflected waves, such that resulting field will be identical to the case when no object is presented. This technique is different to the classical cloaking techniques, where the object is surrounded by the medium, which redirects the beam around the object[45], [46] or creates the opposite to incident field distribution in order to cancel the scattering from this object[47], [48].

This so-called *cloaking metasurface* used in this work is ultrathin (λ/22), has relatively simple design, which makes it easier for fabrication, and works in wide bandwidth and span angle[10].

1.2 Outline

The present thesis consists of two main parts. In the first part, the design, fabrication and experimental analysis of metamaterial lenses are elaborated. Moreover, the experimental results are compared with analytical and numerical results. In the second part, the author's research works on invisibility cloaks are described in detail.

In chapter II we describe materials and methods used in the design and simulation of the metalenses and invisibility cloaks. The simulation tool used and the general procedure followed in the simulation process is depicted. Moreover, the equipment used for experimental verification of the performance of the fabricated devices is described.

In chapter III, the basic aspects and the parameters of the design of a broadband zoned fishnet metalens and a Soret metalens will be presented. In the first part of this chapter, the theoretical principles used (Fermat´s principle) will also be presented. Furthermore, the general optimization procedure followed in the design of the zoned metalens will be depicted. The second part of this chapter is devoted to the Fresnel zones theory and possibility of its combination with the fishnet metamaterial in order to improve radiation characteristics of a lens antenna.

In chapter IV, the design, simulation results and discussion of the carpet cloak based on metasurface with CRR will be presented. Furthermore, the proposed carpet cloak bandwidth and angle span will be characterized.

Finally, the conclusions of the thesis and future work in this field, followed by a summary of the author's merits, are given at the end of this Master Thesis.

2 Chapter II. Materials and Methods

In this chapter, the materials and methods used throughout all this work will be presented. In section 1 we describe the analytical tool based on Huygens-Fresnel principle. In section 2, the main features and a brief description of the electromagnetic simulation tool used will be given. Section 3 focuses on the equipment involved in the experimental verifications.

2.1 Huygens-Fresnel method

In his paper, published more than 300 years ago, Huygens proposed a new mechanism for light propagation[49]. He supposed that in analogy with sound, each point of a wavefront acts as a secondary wave source, see Fig. 2.1.

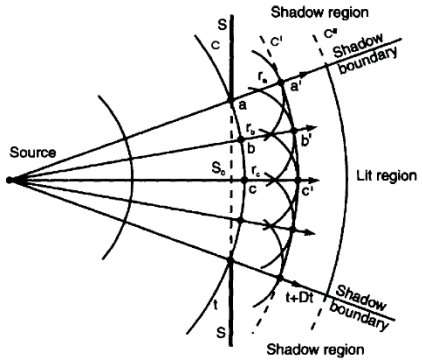

Fig. 2.1. Classical illustration of Huygens' principle. ©2000 Artech House, [50].

Later Fresnel completed this assumption by adding time periodicity, mutual interference and polarization effects into this principle. The resulting Huygens-Fresnel principle became one of the fundamental methods to solve wave diffraction problems.

If we write a spherical wave as:

$$U = U_0 \exp(\mathrm{j}\omega \mathrm{t}) \frac{\exp(-j\,\mathrm{k}_0 \mathrm{R})}{R}, \tag{2.1}$$

where R is distance from the source to the evaluation point, k_0 – wavenumber in free space, ω – angular frequency, U_0 – complex amplitude at the source point, the Huygens-Fresnel principle can be written mathematically as [51]:

$$dU = U_0 K \frac{\exp(-j\,\mathrm{k}_0 \mathrm{R})}{R} dS, \tag{2.2}$$

where K – Kirchhoff diffraction coefficient, S – closed surface.

In order to find the total field it is necessary to integrate over the entire surface *S*. For the sake of simplicity and given the holey nature of the fishnet, we simplify this method by supposing that the holes of the fishnet metamaterial are the only point sources fo the problem. In this case the integral converts into sum of the series of all fields. Also we neglect the Kirchhoff diffraction formula and all reflections and absorptions. Furthermore, all sources have the same amplitude and radiate vertically polarized (E_y) spherical waves, instead of mentioned above spherical waves.

In case of the zoned fishnet metamaterial lens (Section 3.1), it is assumed to be made from isotropic dispersive material with refractive index *n(f)* corresponding to the effective bulk refractive index $n_z(f)$ of the fishnet metamaterial (Fig. 3.1). The phase of each source is calculated as a sum of an incident wave phase and a phase shift in the lens. Then the resulting field in each point of space (*x, y*) is calculated by adding the fields of all sources. Mathematically, this can be written as:

$$A_{x,y} = \sum_{i=1}^{N} \frac{A_i}{\sqrt{l(x,y)}} e^{j(k_0 l(x,y) + k_0 n(f) d_i + \varphi_0)} \tag{2.3}$$

$$l(x,y) = \sqrt{(x - x_i)^2 + (y - y_i)^2} \tag{2.4}$$

where A_i is amplitude of point source *i*; *l(x,y)* is the distance between the point source *i* and point in the space *(x,y)*; k_0 is the wave vector in free space; x_i, y_i are the position coordinates of the holes; *n(f)* is the effective bulk refractive index of the lens; *f* is the operation frequency; d_i is the path inside the lens; φ_0 is the phase of incident plane wave.

In the case of the Soret fishnet metalens (Section 3.2) we use the same method and apply the same equations. The only difference is that now all holes at the output of the fishnet metamaterial have not only the same amplitude but also the same phase.

Despite all assumptions done in the model, such analytical tool demonstrates adequately precise results, which agree well with numerical and experimental results. This allows us to estimate the performance of the designed device in fast and efficient way.

2.2 Simulation tool.

The analytical tool presented in previous section has many advantages and is very helpful for estimation of the performance. However, due to its limitations and many simplifications, this tool cannot provide precise and detailed solution for electromagnetic wave propagation. Such problems can be easily solved by numerical solvers, based on the Finite-Integration Technique (FIT)[52]. In this work we use CST Microwave Studio™[53], which is a fully featured software package for 3D electromagnetic analysis and design in the high frequency range.

CST Microwave Studio™ contains several different simulation techniques (transient solver, frequency domain solver, integral equation solver, multilayer solver, asymptotic solver, and eigenmode solver) to best suit various applications. Each method in turn supports meshing types best suited for its simulation technique. In this work we used transient, frequency domain and eigenmode solvers.

The numerical method (FIT) provides a universal spatial discretization scheme applicable to various electromagnetic problems ranging from static field calculations to high frequency applications in time or frequency domain. In order to solve Maxwell's equations in integral form numerically, a finite calculation domain must be defined enclosing the application problem to simulate. The structure is subdivided applying a mesh generation algorithm with the purpose to discretize the structures to be simulated by many small elements (grid cells), which means that the mesh system used is very important. CST has three available mesh types: *hexahedral*, *tetrahedral* and *superficial mesh*. Depending on the solver type used, some of the mesh types will be available:

- Transient Solver (Time domain solver) → hexahedral mesh.
- Frequency domain solver → hexahedral and tetrahedral mesh.
- Eigenmode solver→ hexahedral and tetrahedral mesh.

In order to save time and computer resources we used the symmetry planes for the design and simulation processes of those structures which had electromagnetic symmetries.

2.3 Equipment

For experimental verification of the fabricated lenses we used a Vector Network Analyzer (VNA) MVNA-8-350-4 (Fig. 2.2), which measures the complex, or vector, transmission and reflection parameters in the millimeter and sub-millimeter frequency domain. It covers the frequency range from 40 GHz up to 1 THz[54].

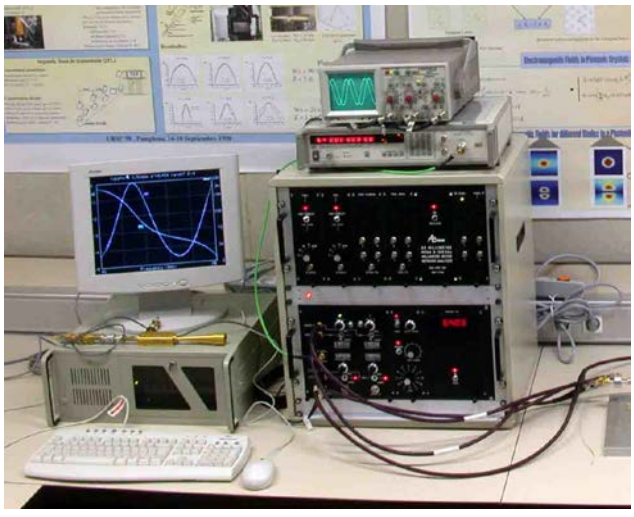

Fig 2.2. MVNA-8-350-4.

The VNA allows to obtain both the amplitude and phase of transmitted and reflected signal. In other words it is possible to obtain complete response of the tested device, which is located in the signal path of the VNA. As sources for different bands it has different MVNA heads – active multiplier chains composed from the sextupler cascaded with an equivalent medium power waveguide amplifiers delivering 40-1000 GHz. Each millimeter head contains a high-efficiency broadband Schottky device, which is electronically tuned over the full frequency range provide the availability of Full Broadband sources for the bands 130-224 GHz, 220-336 GHz, and 660-1000 GHz. In the MVNA's signal path, the measured millimeter wave signal, which reaches the detector head, is converted by a Schottky diode harmonic mixer to much lower frequency. Then, the converted signal is further processed in the heterodyne vector receiver which uses internal reference channel. Receiver frequency tuning is achieved with an internal synthesizer.

3 Chapter III. Metamaterial Lenses

Focusing a wave is one of the most basic tasks of electromagnetism. The device that does this is called a lens and has been employed all along the electromagnetic spectrum, from microwaves to optics. This chapter is dedicated to study two different types of lenses based on fishnet metamaterial. The first lens is a broadband zoned fishnet metalens designed using a combination of the time-honored zoning technique and best fitting procedure. This combination allows one to reduce the profile of a fishnet metamaterial lens and maintain a relatively broadband regime. The second part of this chapter is dedicated to a Soret fishnet metalens, which is designed using the principles of Fresnel zones and corresponds to the family of Fresnel zone plates. It is shown that by combining the Fresnel zone plate with a fishnet metamaterial, the performance of the device can be improved.

3.1 Broadband zoned fishnet metamaterial lens.

As it was mentioned in Chapter I, among all practical realizations of metamaterials, the fishnet metamaterial, i.e., stacked subwavelength hole arrays, has become the strongest candidate for frequencies beyond microwaves because of its lower losses compared to other metamaterial structures and frequency-robust magnetic response[31]. Hence, plano- and bi-concave fishnet lenses have been designed for millimeter-wave applications[32]–[34] demonstrating a good performance. However, these lenses are still relatively voluminous and heavy for practical implementations. In order to overcome these drawbacks, the time-honored zoning technique can be applied, so that redundant wavelength phase shift material is removed[12], [51], [55]. Alike zoned metallic[12] and optical dielectric lenses, also known as Fresnel lenses[50], [51], this modification results in a fishnet metamaterial lens with low thickness and, therefore, reduced weight and absorption losses[35], [36]. The outcome is then a diffractive optical element akin to Fresnel zoned metallic plate lenses [50], [51] but with an enhanced impedance matching.

3.1.1 Design and fabrication

Fishnet metamaterial.

A unit cell of the fishnet metamaterial used for this lens has the following dimensions: d_x = 2.5 mm, d_y = 5 mm, d_z = 1.5 mm and thickness of the metallic plate w = 0.5 mm (see inset of Fig. 3.1). The index of refraction n_z for an infinite number of plates (i.e. the bulk refractive index) is calculated using the Eigenmode solver of the commercial software CST Microwave Studio™, applying periodic boundary conditions in all planes. In this analysis the metal is modeled as a perfect electric conductor (PEC). As shown in Fig. 3.1 (black curve) the bulk refractive index is negative between 53 and 58 GHz and strongly dispersive. In addition, the effective refractive index of structures with a finite number of plates can obtained using the standard retrieval method from the S-parameters [56]. These are obtained using the frequency domain solver of CST Microwave Studio™, with unit cell boundary conditions and modelling the metal as aluminum (σ_{Al} = 3.56×107 S/m). The effective refractive index for several plates is shown in Fig. 3.1. Since

the fishnet metamaterial with only a few plates cannot be treated as a homogeneous medium the effective index deviates from the infinite structure calculation. This can be clearly observed in Fig. 3.1, where the effective index for two plates (dash-dot blue curve) does not converge to the bulk index. Obviously, as the number of plates increases the disagreement reduces rapidly. Hereby, it can be concluded that a relatively large number of plates is preferable to minimize the deviations of the effective refractive index with the number of stacked plates. However, this would result in undesirable increased thickness and losses. From previous experience (also it can be seen in Fig. 3.1), beyond four stacked plates (dashed red line) there is a good convergence with the bulk index, especially within the range 54-56 GHz. So an initial stack of 4 plates is a good trade-off[32]–[35], [57] to maintain both thickness and losses low while the effective refractive index is not significantly altered with the addition of some additional stacked plates to reach the zoned profile.

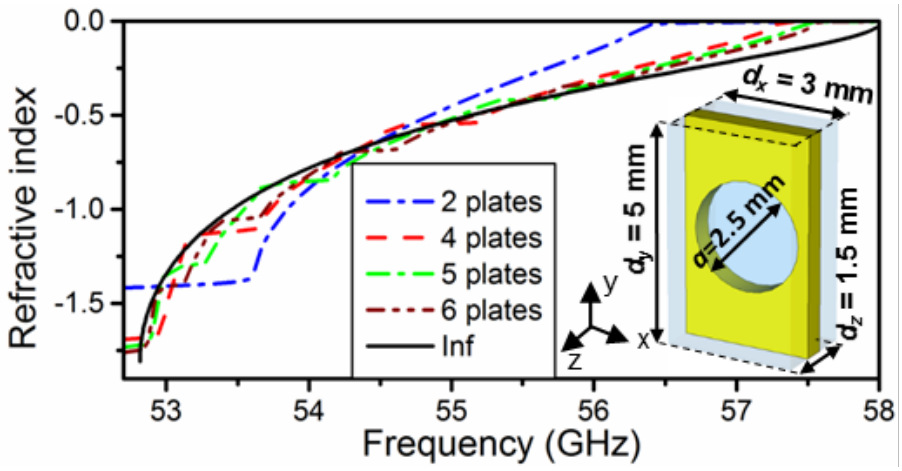

Fig. 3.1. Effective refractive index, n_z, for a fishnet metamaterial made of 2 (blue dashed-dot curve), 4 (red dashed curve), 5 (green dashed-dot curve), 6 (brown dashed-dot-dot curve) and infinite number of plates (black solid curve). Dimensions of fishnet metamaterial unit cell (Inset).

Design procedure

Before applying the zoning technique, we first describe a profile of non-zoned lens (Fig. 3.2), which follows an analytical curve, derived from the Fermat's principle [34]:

$$\sqrt{\left(f-a\right)^2+b^2}\cdot n_0 + a\cdot n_z = f\cdot n_0 \tag{3.1}$$

where f is a focal length, n_0 is refractive index of the free-space and n_z is the index of refraction of the lens medium.

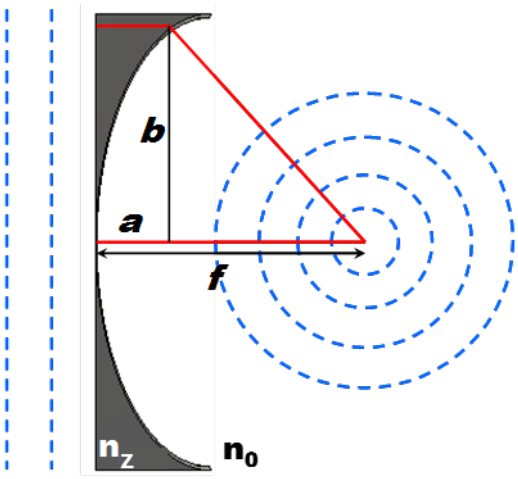

Fig. 3.2. Illustration of Fermat's principle for a non-zoned lens profile.

From this equation it can be noticed that the profile of the lens takes different forms, depending on the value of n_{lens}. So as an interesting outcome, for the values of $n_{lens} < 1$ the resulting profile of the lens is concave instead of the usual convex profile of traditional dielectric lenses. Particularizing to negative index values, it is easily demonstrated that for $n_{lens} < -1$ the lens profile is a hyperbola, for $n_{lens} = -1$ is a parabola and for $-1 < n_{lens} < 0$ it takes the form of an ellipse. In our case, the effective index of the fishnet metamaterial lays between -1 and 0, and thus the profile of the non-zoned lens must be an ellipse.

In the next step, in order to find the smooth zoned lens profile we apply the well-known zoning technique, which implies the removal of material each time a 2π phase shift is reached. The thickness of this layer t can be calculated as [12]:

$$t = \frac{\lambda_0}{1 - n_z}, \tag{3.2}$$

where λ_0 is the free-space wavelength and n_z is the index of refraction of the medium. By combining (3.2) with (3.1), the design equation is as follows [35]:

$$\left(1 - n_z^2\right)\left(z + mt\right)^2 - 2\left(FL + mt\right)\left(1 - n_z\right)\left(z + mt\right) + x^2 = 0, \tag{3.3}$$

where n_z is the effective refractive index of the structure, FL is the focal length, and m is an integer ($m = 0, 1, 2, 3$) that represents the successive steps for the zoned lens profile. The successive steps for the zoned lens profile and thickness limits for two demonstrative frequencies $f_1 = 54$ GHz and $f_2 = 55.5$ GHz are shown in Fig. 2.3. It is obvious that the equation (3.3) contains two frequency-dependent components: the thickness of the zoned lens t and, since the fishnet metamaterial is highly dispersive, the refractive index n_z.

The simultaneous dependence of the design equation on two parameters (frequency and focal length FL) makes it possible to find the profiles for two different frequencies, whose curves coincide, by simply selecting the appropriate focal lengths. As a result, we obtain one zoned lens

profile for two different frequencies and focal lengths, as is demonstrated in Fig. 3.3 (solid black line).

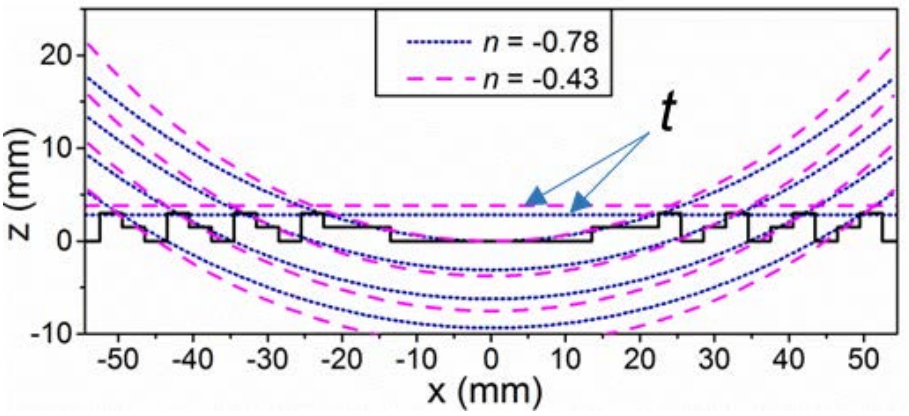

Fig. 3.3. Lens profiles and curves of the successive steps for: n_{z1} = -0.78 (dotted blue curve) and for n_{z2} = -0.43 (dashed pink curve) along with the values of the thickness limits, t_1 and t_2 (blue and pink horizontal curves, respectively).

Due to the discretization imposed by periods of the fishnet metamaterial d_x and d_z, the zoned yet smooth profile should be approximated by a staircase profile (see Fig. 3.3). As a criteria of a good fitting we use the root-mean-square-error (RMSE) between the smooth profile and the staircase approximation. In order to obtain the optimal lens profile, which provides the broadband performance, a best fitting procedure to minimize RMSE is done for the whole operation band. Notice that the effective refractive index of an infinite fishnet metamaterial is used for this analysis (black curve in Fig. 3.3). Due to the intrinsic dispersion of the fishnet structure, each frequency has only a unique optimal profile. So, for broadband operation a trade-off solution must be found. Therefore, as a result of this smart engineering procedure – combination of zoning technique and dispersion – the optimal zoned lens profile is obtained, see Fig. 3.3 (solid black curve). Notice that since there are many combinations of frequency and focal lengths it is possible to find several zoned lens profiles, whose RMSE is low.

The resulting RMSE for our optimal profile is plotted in Fig. 3.4(a) as a function of frequency/effective bulk refractive index and focal length. From Fig. 3.4(a) it can be seen that RMSE has low values for the whole spectral window of interest demonstrating broadband regime. It should be noticed that the resulting lens profile is completely different from that used in previous works[35], [36], where it was obtained by applying the zoning technique only for a single frequency, without applying best fitting procedure. As a result, the RMSE for a single frequency (f = 56.7 GHz) lens (see Fig. 3.4(b)) has low values for a narrower band. From Fig. 3.4(a) it can be seen that the relative minimum of the RMSE follows a parabolic-like trend starting from FL = 41 mm at 53 GHz and reaching the top end of the color map FL = 65 mm around 58 GHz. This trend is a direct consequence of the strong dispersion of the fishnet metamaterial (see Fig. 3.1) that causes chromatic aberration for the fishnet lens [32]–[34]. According to Fig. 3.4(a), the absolute minimum RMSE is obtained for f = 53.5 GHz and FL = 45 mm. However, from Fig. 3.1

we know that the convergence of the effective bulk refractive index for infinite and finite numbers of plates is poor at that frequency. Therefore, poor performance at this frequency is expected. Observing Fig. 3.1, it is noticed that the best convergence happens in the interval 54-56 GHz. For this reason, for illustrative purposes we choose the frequencies at approximately both ends: f_1 = 54 GHz and f_2 = 55.5 GHz. At these frequencies, the effective bulk refractive index is n_{lz1} = -0.78 and n_{z2} = -0.43, respectively.

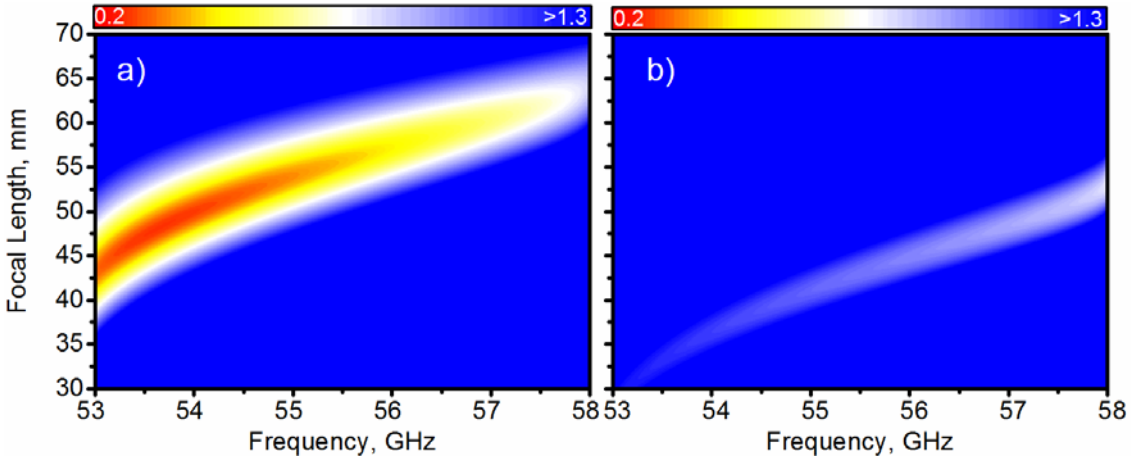

Fig. 3.4. Color maps of RMSE of the zoned lens profile as a function of frequency and focal length for (a) broadband zoned fishnet metamaterial lens and (b) single band zoned fishnet metamaterial lens.

At f_1 = 54 GHz and focal length FL_1=48.7 mm (8.8λ_1) the RMSE is δ_1= 0.22 mm. Such error can lead to a shift of the focus δFL_1 = - 0.7 mm (0.23$\lambda_1 \approx$ 2%) because of the staircase approximation imposed by the fishnet metamaterial. In another words, the staircase approximation of the continuous profile can follow another profile with different focal length, causing the shift of the focus. At the second frequency f_2 = 55.5 GHz and focal length FL_2 = 55 mm (10.2λ_2) the RMSE is δ_2 = 0.44 mm and may result in a slightly larger focus shift δFL_2 = -2.3 mm (0.4$\lambda_2 \approx$ 4%). The curves defined by (2) for four successive steps (m = 0, 1, 2, 3) at the two considered frequencies are shown in Fig. 3.3(b): f_1, dotted blue lines; f_2, dashed pink lines. Also, the maximum thickness[12], [35], [36] for each frequency, t_1 = 2.8 mm (0.5$\lambda_1 \approx 2\ d_z$) and t_2 = 3.8 mm (0.7λ_2), are represented by horizontal dashed blue and pink lines, respectively.

Since one and two plates are necessary to realize the three-level binary profile, see Fig. 1(b), and four plates are the minimum for the central part (due to inhomogeneity of fishnet metamaterial), the total thickness of the lens results in $5d_z+w$ = 8 mm (1.4λ_1). Along x and y directions the structure consists of 37 d_x and 27 d_y periods, respectively. Therefore, the final design has total dimensions of 111 mm × 135 mm × 8 mm (19.8λ_1 × 24.1λ_1 × 1.4λ_1) without the frame used to facilitate the assembly. The fabricated zoned fishnet metamaterial lens is shown in Fig 3.5.

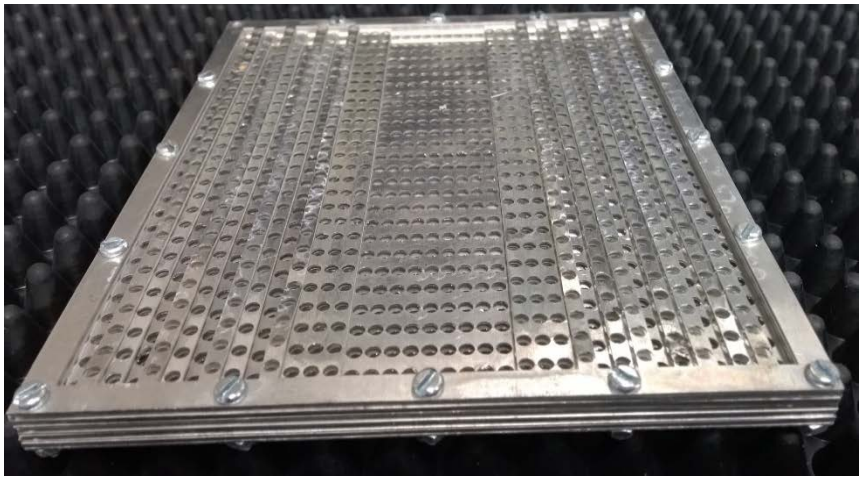

Fig. 3.5. Photo of fabricated broadband zoned fishnet metamaterial lens.

3.1.2 Analytical and Simulation Results

First, using the Huygens-Fresnel method described in Chapter II, the analytical power distribution is calculated as a function of frequency and position along the optical axis of the lens (Fig. 3.6(a)).

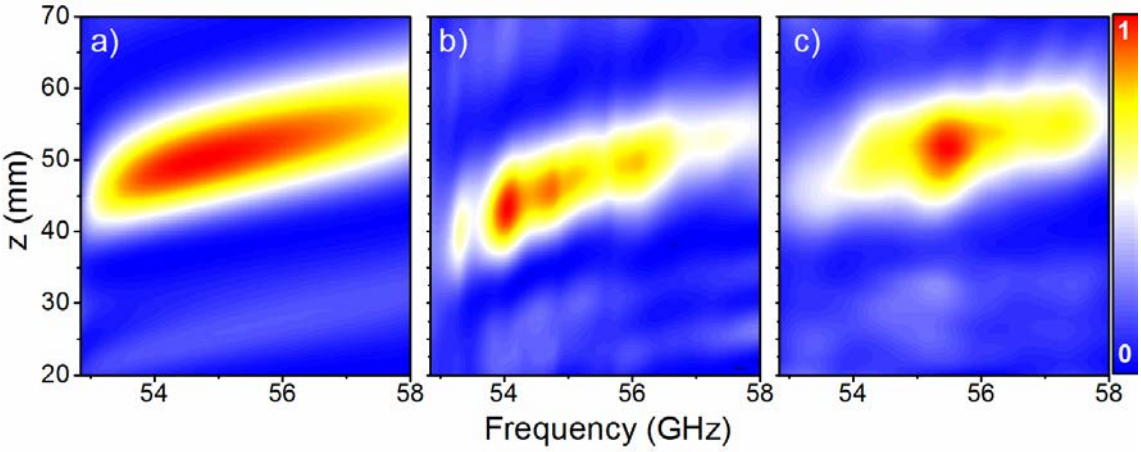

Fig. 3.6. Power distribution along *z* axis for the frequency range 52–58 GHz: (a) analytical results, (b) experimental and (c) simulation results.

A broadband operation is observed, with a band extending from 53.5 GHz (*FL* = 45 mm) to 58 GHz (*FL* = 56 mm) with the absolute maximum power located between 54-56 GHz, in good agreement with the RMSE calculation. In Fig. 3.6(a) one can notice that, alike other diffractive optical elements [50], [51], there are secondary foci. For the frequency span shown, a secondary focus moving within the z-range 20 to 35 mm is visible. This secondary focus is however significantly lower in amplitude than the main focus. As next step, the spatial power distribution on the *xz*-plane for the two frequencies is presented in Fig. 3.7(a): f_1 = 54 GHz (top) and f_2 = 55.5 GHz (bottom). For both frequencies, clear foci can be observed with half-wavelength resolution. Also, prominent side lobes are noticeable off-axis surrounding the focus. Nevertheless, they emerge at significant different distance than the focal plane.

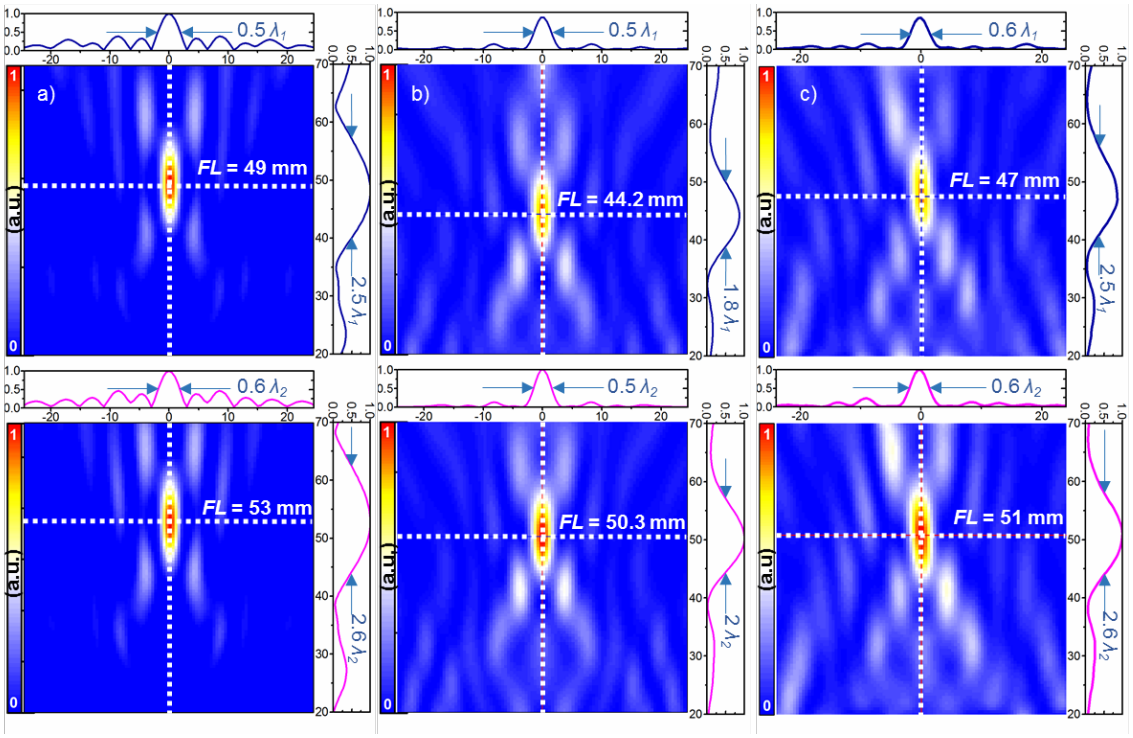

Fig. 3.7. Analytical (a), experimental (b) and simulation results (c) for of the spatial power distribution on the *xz*-plane for: (top) f_1=54 GHz and (bottom) f_2=55.5 GHz. The normalized power distributions along *x*-axis (at each focal length) and along the optical axis are represented in each panel on the top- and right-side plots, respectively.

Next, a full-wave numerical analysis of the realistic 3D model of the zoned lens is done using the transient solver of the commercial software CST Microwave Studio™. The bulk conductivity of aluminum (σ_{Al} = 3.56×10^7 S/m) is considered for the modeling of the fabricated fishnet metamaterial lens. A fine hexahedral mesh is used with minimum and maximum mesh cell sizes of 0.125 mm (0.02λ_1) and 0.28 mm (0.05λ_1), respectively. A vertically polarized (E_y) plane wave is used to excite the lens, impinging normally on its planar face. Perfectly matched layers ("open add space") are used in the boundaries of the simulation box to emulate a lens in free space. Given the two-fold symmetry of the problem, electric and magnetic mirror planes are placed in the *xz*- and *yz*-planes, respectively, with the aim to reduce computation time. The simulation is run for a sufficiently long time to ensure that the continuous-wave information computed by Fourier transformations is valid. Although time consuming, and thus, undesirable for a fast prototyping (unlike the Huygens-Fresnel principle), the results derived from this approach should obviously have a better agreement with the experimental ones.

Initially, the power distribution as a function of *z* position and frequency is obtained by placing *E*-field and *H*-field probes, instead of an open-ended WR-15, along the optical axis (*z*-axis) with a 0.5 mm step. These probes record the waveform at their positions and by Fourier transformation, the *E*- and *H*-field spectra are obtained. The resulting power distribution is shown in Fig. 3.6(b). The focal spot is located in the frequency range 53.5-56.5 GHz and moving from

42 up to 51.5 mm along *z*-axis. This result resembles the analytical distribution. The dark red spot accounting for the maximum power is concentrated within a narrower frequency band.

Then, the *xz*-maps of power distribution generated from the simulation for f_1 = 54 GHz and f_2 = 55.5 GHz are plotted on the top and bottom color maps in Fig. 3.7(b), respectively. These color maps bear a resemblance to analytical results. In particular, they model more accurately than the analytical approach the relative amplitude between the main focus and the side lobes.

In the next step, in order to confirm the broadband performance of the zoned lens, the enhancement as a function of frequency is compared to the enhancement of a zoned fishnet metamaterial lens optimized for single-band operation, already reported in our previous works [35], [36]. The numerical results are obtained using the same full-wave numerical analysis of the realistic 3D model and are shown in Fig. 3.8. The zoned lens discussed here exhibits an enhancement above 9 dB for the whole negative refractive index band and has a maximum at the frequency f_1= 54 GHz, which is in good agreement with Fig. 3.4(a) where RMSE is minimal at this frequency. The zoned lens optimized for single-band operation, in turn, achieves enhancement values above 9 dB only at the design frequency range, 55 - 56.5 GHz, also in agreement with Fig. 3.4(b).

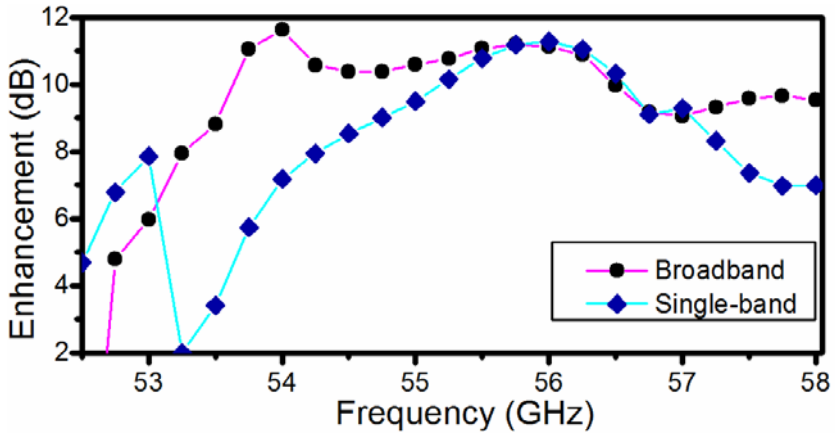

Fig. 3.8. Numerical results for the enhancement as a function of frequency for the single-mode zoned lens (red curve) and for the broadband zoned lens (blue curve.

Finally, the free-space matching is estimated by obtaining the reflectance for the full structure. The reflectance R is defined as the ratio of the reflected power P_{refl} and the incident power P_{inc}, $R = P_{refl}/P_{inc}$. The incident flux P_{inc} is calculated without the lens, in order to avoid any contribution of reflected power. The reflected power P_{refl} is calculated from sum of power flux located before the lens $P_{st} = P_{inc} - P_{refl}$. Given the z normal planes at which we compute P_{st} and P_{inc}, and that the lens is illuminated with a linearly polarized plane wave, we consider only the z-component of the power flux. The obtained reflectance R for the frequencies 52.5-58 GHz is shown in Fig. 3.9(b). As it is expected from the dispersion diagram (Fig. 3.1), below 53 GHz the reflectance R is significantly high. At the chosen illustrative frequencies, R is 0.26 and 0.43 for

the lower and higher frequency, respectively. One can notice the agreement with Fig. 3.6(b), where the maxima are at 54 GHz and 54.75 GHz. When comparing the reflectance of the zoned fishnet metamaterial lens with a zoned lens made of Silicon (dashed grey line), a material widely used for lenses at millimeter-waves and terahertz [58], [59], it is evident that the lens analyzed here outperforms the Silicon counterpart in terms of Fresnel reflection losses for ~54 – 55. 5 GHz. This frequency range coincides with the band where good convergence of effective refractive index among different number of stacked layers was observed, see Fig. 3.1.

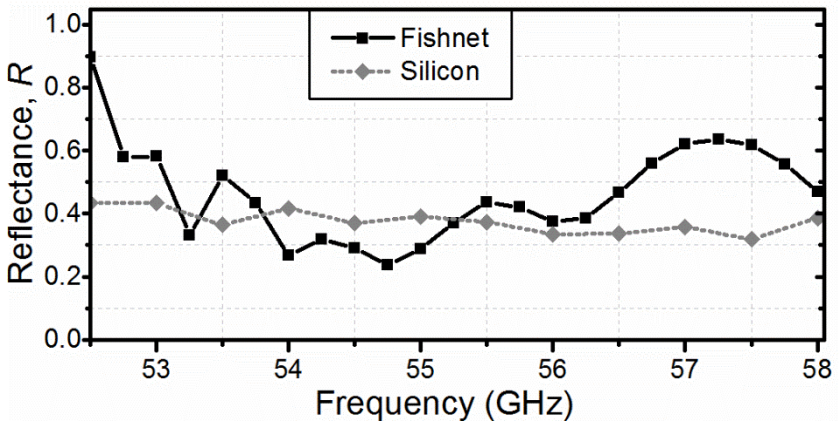

Fig. 3.9. Reflectance for the zoned fishnet metamaterial lens (solid black line) and the Silicon zoned lens (dashed grey line).

3.1.3 Experimental verification.

The experimental characterization is done using an AB Millimetre™ quasi-optical vector network analyzer with the setup illustrated in Fig 3.10. To illuminate the lens, a V-band corrugated horn antenna is placed at a distance L= 3300 mm from the lens. At this distance the radius beam waist of the Gaussian beam is ~400 mm for both working frequencies, which ensures a uniform illumination of the lens. An open-ended rectangular waveguide (WR-15) is used as a detector, for the *xz* raster scanning. Millimeter-wave absorbers are used throughout the setup to mimic anechoic chamber conditions. The calibration is done by recording the transmitted power without the lens. For the power distribution as a function of frequency and *z* position, the lens is placed in the setup and the detector is moved from 20 to 70 mm away from the lens along *z*-axis (with 0.5 mm steps) while recording the spectrum in the range 50-60 GHz. Similarly, *z*-frequency- and *xz*-maps are generated experimentally using the prototype described previously (Fig. 3.10).

First, analogously to the previous methods, the power distribution is obtained as a function of frequency and z position. The color map is shown in Fig. 3.6(c), which resembles that obtained following the Huygens-Fresnel principle and obtained in the simulations (Fig. 3.6(a-b)). This color map is obtained after applying a Butterworth low pass filter, in order to minimize the ripples in the experimental data caused by the excitation of standing waves between the lens and the detector (demonstrated in the simulation results of next section but not shown here). In this figure, the broadband performance of the zoned lens from 54 GHz to 58 GHz can be observed, with some penalty in performance for extreme frequencies, which is in good agreement with the

results obtained by the Huygens-Fresnel principle and numerical results. The maximum power enhancement (i.e., the ratio between the intensity with and without lens for each *xz* position) is 10.5 dB at 54 GHz and 13.1 dB at 55.5 GHz. These maxima occur at z = 47 mm and 51 mm, respectively. It is also noticeable a secondary focus at around 30 mm for 55 GHz. Further, the power is scanned on *xz*-plane at frequencies f_1 = 54 GHz and f_2 = 55.5 GHz. The results of the spatial power distribution are shown in Fig. 3.7(c), for f_1 (top) and f_2 (bottom), respectively. A good qualitative agreement with the analytical as well as simulation results is evident.

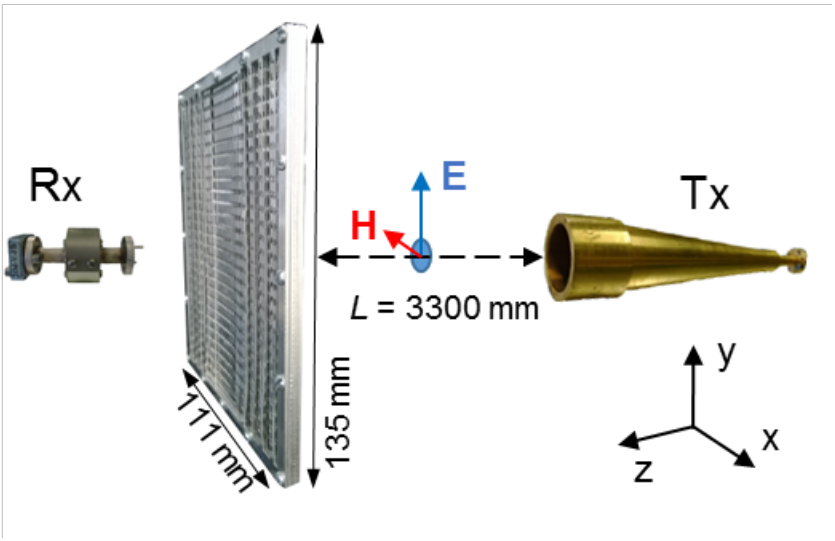

Fig. 3.10. Sketch of the experimental setup. Tx and Rx stand for transmitter and receiver, respectively.

3.1.4 Lens antenna configuration

Finally, after fully characterizing the zoned lens, we investigate its performance in a lens antenna configuration. To this end we use again the AB Millimetre™ quasi-optical vector network analyzer using a similar setup, but an open-ended WR-15 is used now as a feeder placed at the experimentally-computed focal length of each frequency. In order to measure the angular distribution of the radiated power, the feeder and the zoned lens stand on a rotating platform that rotates from -90 deg to +90 deg with 1 deg step. A high gain standard horn antenna is placed 3650 mm away from the flat face of the zoned lens to detect the radiated power. Notice that, strictly speaking, the detection is not done in far-field according to the convention $z_{ff} = 2D^2/\lambda$, where D is the diameter of the lens: for f_1 = 54 GHz, z_{ff1} = 4435 mm and for f_2 = 55.5 GHz, z_{ff2} = 4560 mm. Nevertheless, it should give us a good approximation. Absorbing material is also used throughout the setup for reflection suppression. The obtained co- and cross-polar angular measurements for f_1 = 54 GHz and f_2 = 55.5 GHz are displayed in Fig. 3.11. For f_1 [Fig. 3.11(a)], the main lobe has half-power beamwidth (HPBW) and first null beamwidth (FNBW) of 3.5 deg and 40 deg, respectively, with a side lobe level (SLL) of 5.7 dB at around ±8 deg. It can be demonstrated that this side lobe corresponds to the (0,-1) grating lobe of the periodic holey pattern [36]. An additional minor lobe can be seen at ±65 deg. In this case, it is caused by the spillover [36] and can potentially be eliminated by increasing the lateral size of the lens. The results for f_2 (Fig.

3.11(b)) are similar. The main lobe has HPBW= 4.3 deg and FNBW = 39 deg, respectively, with SLL = 6.7 dB at around ±7 deg. The spillover lobe occurs at ±65 deg. The maximum directivity estimated using the method described in Ref. [60] is 16.6 dBi and 15.6 dBi for f_1 and f_2, respectively. The cross-polar level is ~25 dB and ~40 dB for f_1 and f_2 respectively, indicating the good performance of the zoned lens antenna. Arguably, the measured cross-polar level might be originated from experimental misalignment, since the on-axis cross-polar should vanish for a perfectly symmetric configuration about the *yz*-plane, as the simulations described below confirm. The non-negligible cross-polar measured at ±65 deg arises evidently from the spillover.

Radiation parameters have also been modeled numerically. An open-ended WR-15 feeder is placed at the numerical focal length of each frequency and the radiation pattern is calculated at the same distance as in the experiment z_{ff}=3650 mm. The co-polar results are plotted as well in Fig. 3.11 to facilitate the comparison with the experiment. The numerical cross-polar, however, is not plotted given its negligible value. One can see that the radiation patterns for numerical calculations are similar to experimental results. The main lobe has HPBW = 3.2 deg and FNBW = 40 deg for f_1, and HPBW = 4.1 deg and FNBW = 56 deg for f_2. The first side lobes and the spillover lobe appear at similar angles, but with lower levels than in the experiment. The maximum directivity, which can be computed readily from the simulation, is 15.4 dBi for f_1 and 15.2 dBi for f_2, which is in good agreement with values estimated from experimental results.

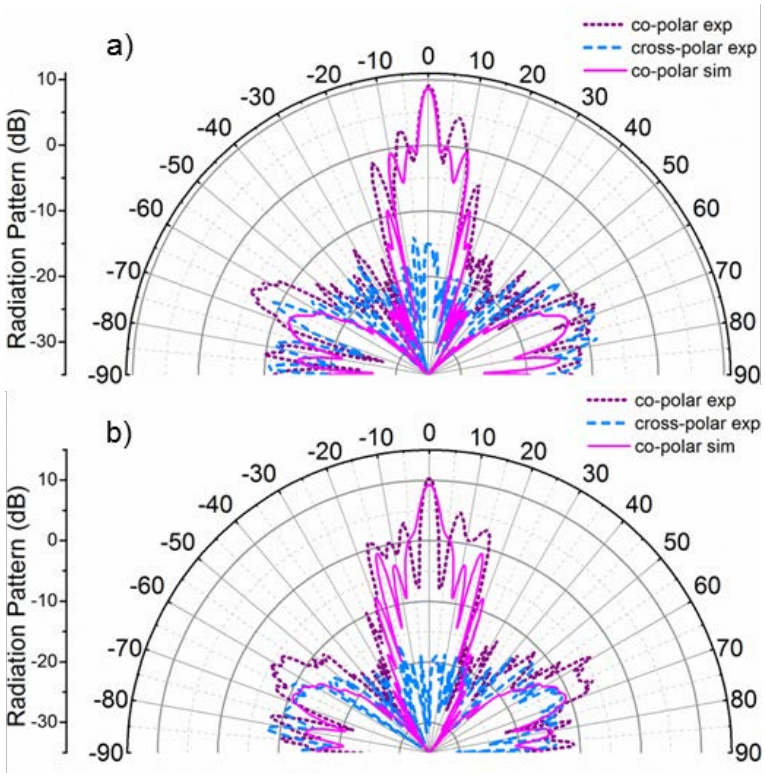

Fig. 3.11. H-plane (*xz*-plane) radiation pattern for: (a) f_1=54 GHz and (b) f_2=55.5 GHz. Dashed and solid lines represent experimental and numerical results, respectively. Purple and blue colors stand for co- and cross-polar data, respectively.

To facilitate the comparison, all main focal properties for the three methods investigated are gathered in Table I. It is shown that the results are also in good agreement quantitatively with each other and with the designed values based on ray tracing approximation. Only, the FWHM show minor disagreement between measurements and both analytical and numerical calculations. This can be arguably ascribed to the non-subwavelength nature of the detector used in the experiment (an open-ended waveguide, WR-15), which averages the field strength.

TABLE I. Results of the zoned lens

	FL_1[1], mm	FL_2, mm	$FWHM_1$[2], mm	$FWHM_2$, mm	DF_1[3], mm	DF_2, mm
Analytical	49	53	3	3	14	13.8
	$8.8\lambda_1$	$9.8\lambda_2$	$0.5\lambda_1$	$0.6\lambda_2$	$2.5\lambda_1$	$2.6\lambda_2$
Experimental	47	51	3.3	3.4	13.7	14.2
	$8.4\lambda_1$	$9.4\lambda_2$	$0.6\lambda_1$	$0.6\lambda_2$	$2.5\lambda_1$	$2.6\lambda_2$
Simulation	44.2	50.3	2.8	2.8	10	10.7
	$7.9\lambda_1$	$9.3\lambda_2$	$0.5\lambda_1$	$0.5\lambda_2$	$1.8\lambda_1$	$2\lambda_2$

[1]FL is the focal length.
[2]FWHM is the full width at half maximum.
[3]DF is the depth of focus.

For the analytical results, the deviations of the focal positions from designed values are less than 2%, which is included into the error of the zoned lens profile. The experimental results show deviations of focal length below 6%. These discrepancies fall perfectly within the experimental error caused by misalignments and defects of the fabricated zoned lens. As for simulations, the deviations are less than 9.5%. It is worth noting that for the initial design based on ray tracing, the lens is assumed to be isotropic with refractive index extracted from the infinite-layered fishnet structure. Hence, it is reasonable to expect a good agreement between the experimental and numerical results, where the anisotropic nature of the fishnet is fully considered. The Huygens-Fresnel principle is more similar to the ray tracing design, where the lens is assumed isotropic, therefore, the analytical results obtained with this method deviate more from experimental and numerical results.

Thereby, the good agreement observed between all approaches validates the good performance of the lens for frequencies from 54 GHz to 58 GHz. Also, these results demonstrate that, despite all the assumptions used for the Huygens-Fresnel principle, it can be well used initially for a fast prototyping.

3.2 Soret fishnet metalens

Another metamaterial lens which has been designed, fabricated and analysed is a Soret lens, member of the Fresnel-zone plate lens (FZPL) family. This lens consists of alternating transparent and opaque concentric rings[61]. At the beginning this lens was considered as a purely optical device. Ultimately, the same concept has been successfully applied throughout the whole electromagnetic spectrum and in particular in the microwave range for lens antennas[50], [51], [55]. At microwaves these lenses present interesting characteristics such as low profile, low cost and ease of fabrication.

However FZPLs in microwave regime have a low efficiency in transmission compared to conventional lenses, due to the fact that half of the incident energy is reflected from opaque zones. This low focusing efficiency also deprecates the radiation efficiency of antenna applications, such as Fresnel-zone plate antennas (FZPA), making them less competitive than other conventional antennas. Another drawback is that the best performance of FZPA is normally obtained for large focal distance/diameter ratio ($F/D \sim 3\text{-}15\lambda$)[50]. Thus, the volume enclosing the Soret lens along with the feeder is very large, making FZPA not suitable for compact systems. This leaves original FZPL and FZPA attractive only for few niches such as broadcast satellite reception[50].

The performance of FZPL and FZPA can be improved by an advanced design, which reduces the amount of reflected power, i.e. improves the efficiency, by introducing selective phase shifts instead of blocking negative (odd) or positive (even) Fresnel zones[50], [51]. This smart approach leads to high gain, aperture efficiency and low side lobe level[62]. However, this increases the thickness and complicates the design and, as a result, the fabrication and cost.

Another possible way to improve the performance of the FZPA is to replace the transparent rings of the Soret lens by subwavelength hole arrays, which allows the excitation of surface currents (leaky-waves) and could improve coupling-in and -out of the spatial wave as it happens in the extraordinary transmission phenomenon[63]. Moreover, by introducing at the input of the FZPA a metamaterial slab with near zero index (NZIM) it is possible to increase the directivity of the antenna and reduce the sidelobe level, since the phase front at the output surface of the NZIM follows its shape and therefore the electromagnetic field becomes locally closer to a plane-wave distribution[64]–[66]. Recently, the fishnet metamaterial (i.e. closely-packed subwavelength hole arrays working under extraordinary optical transmission[24], [28], [63] and emulating NRI and NZIM) was proposed for advanced lens design[32], [34], [35]. Their performance in the microwave regime has been confirmed in previous works[32], [34]–[37], [57]. Alike the single holey plate exhibiting extraordinary transmission, the leaky-wave mechanism present in the fishnet metamaterial may facilitate the coupling-in and –out, guaranteeing then a low insertion loss[28], and may improve the effective illumination and extend radiating area[29], increasing the total efficiency of the lens antenna. This increased illumination efficiency allows a comparatively smaller F/D ratio, which means that the volume of FZPA can be reduced, by placing the transmitter closer to the FZPL. Another advantage of the fishnet metamaterial is the

possibility to tailor an effective impedance matched with the free space, in the desirable NZIM regime.

3.2.1 Design and fabrication

Fishnet metamaterial.

The unit cell of the fishnet metamaterial used for this lens (inset of Fig. 3.12) is designed using the commercial substrate Rogers RO5880™ and has the following dimensions: d_x = 1.26 mm, d_y = 2.1 mm, d_z = 0.398 mm (metal thickness w = 0.017 mm and thickness of dielectric t_d = 0.381 mm), hole diameter $a = d_y/4$ = 0.525 mm and spacer dielectric permittivity ε_r = 2.2, with loss tangent $\tan\delta = 9\times10^{-4}$. For these parameters, the cut-off frequency of the hole fundamental TE_{11} mode is 112 GHz. The dispersion diagram of the infinite structure is numerically calculated using the commercial software CST Microwave Studio™, using the same procedure described in Section 3.1.1 of this chapter. The first band appears at 87-96 GHz, as shown by the black dash-dotted line in Fig. 3.12, and corresponds to the fishnet extraordinary transmission band. However, the calculation for a finite number of plates deviates from the infinite structure curve due to the inhomogeneity of the fishnet metamaterial. In Section 3.1.1 of this chapter we found that four plates is a good trade-off between total thickness and electromagnetic performance in terms of insertion loss.

In order to obtain the effective refractive index of the fishnet metamaterial, consisting of 4 periods with periodicity d_z, we use now the phase of the electric field inside the structure (assuming that the transmittance is high), by exploiting the frequency domain solver in the range 90-110 GHz. Unit cell boundary conditions were used and the metal was modelled as aluminium ($\sigma_{Al} = 3.56\times10^7$ S/m). A fine tetrahedral mesh is used, with minimum and maximum edge lengths of 0.007 mm (~$0.003\lambda_0$) and 0.64 mm (~$0.2\lambda_0$), respectively.

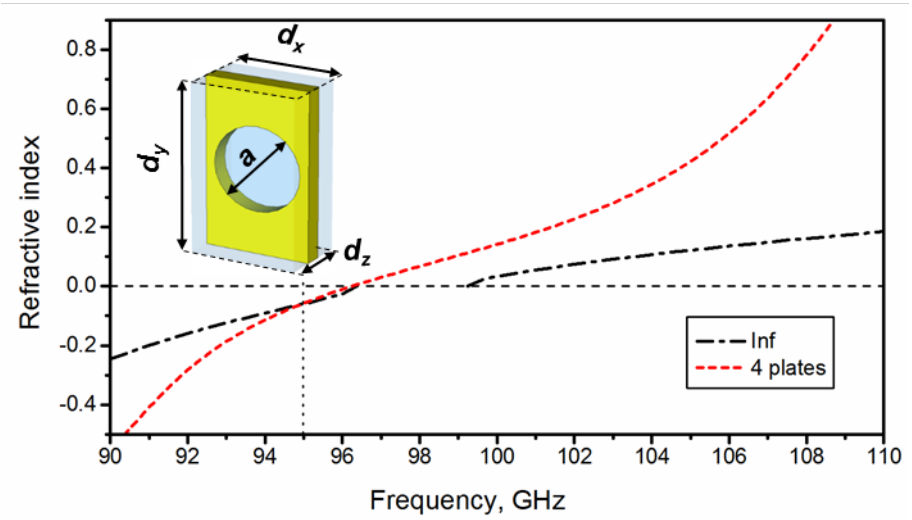

Fig. 3.12. Effective refractive index of fishnet metamaterial for infinite number of plates (black dash-dotted line) and four plates (red dashed line). Dimensions of unit cell (Inset).

The resulting effective index of refraction can be calculated as:

$$n_z = \frac{\Delta\varphi}{k_0 \Delta d}, \tag{3.4}$$

where Δφ is the phase variation in the thickness Δ*d* and k_0 is wave number in free-space. The resulting effective index of refraction for 4 cascaded plates is shown in Fig. 3.12 (red dashed line). As it can be noticed, the bandgap between 97 and 99 GHz due to Wood's anomaly disappears in this case. This is more evident in the transmission coefficient S_{21} for 4 cascaded plates, shown in Fig. 3.13. This feature has been observed before and is due to the tunneling of energy when the number of plates is small. As it was said before, we want the fishnet metamaterial to behave as NZIM, so we choose 95 GHz (λ_0 ~ 3.16 mm) as design frequency where the index of refraction is n_z = -0.06.

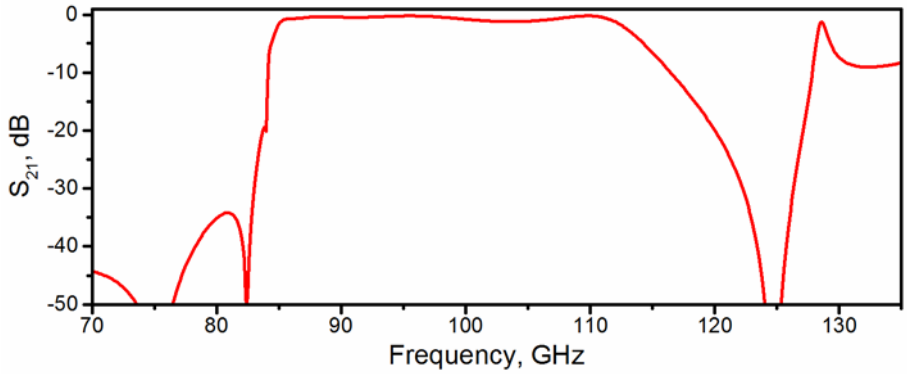

Fig. 3.13. Transmission coefficient for a four-plate fishnet metamaterial.

Soret lens design

Once we have defined our fishnet metamaterial we design a Soret lens. The radii of the Fresnel zones r_i of the Soret lens can be found using the classical design equation [50], [51], [55]:

$$r_i = \sqrt{\frac{2FL \cdot \lambda_0 \cdot i}{p} + \left(\frac{i \cdot \lambda_0}{p}\right)^2} \tag{3.5}$$

where *FL* is the focal length of the FZPL, λ_0 is the operation wavelength, *i* is an integer denoting zone number and *p* = 2, 4, 6… is the number of phase quantization levels.

The positive (odd) zones were made of holes of the same dimension as the fishnet, while the negative (even) zones remain without holes. Since the fishnet metamaterial unit cell size (with in-plane periods d_x and d_y) is comparable to the free space wavelength, it is also comparable to the radii of the Fresnel zones. This restricts the possible combinations of the parameters. For example the number of phase quantization levels *p* can be only equal to 2, since with *p* higher than 2 the transparent zones will become too narrow compared to one unit cell. Therefore, the performance of the Soret fishnet metalens depends on the filling ratio of the Fresnel zones. This, in turn, depends on many parameters of the design, such as *FL*, λ, *i*, *p*.

In order to quickly and easily estimate the performance of the designed FZPL, we used a three-dimensional analytical calculation using the Huygens-Fresnel principle, which was previously described in Chapter II. Here it should be noticed that, unlike traditional designs, a subwavelength focal length $FL = 0.5\lambda_0 = 1.58$ mm was chosen to demonstrate the possibility of designing very compact systems. In order to improve the aperture efficiency, or equivalently the illumination efficiency, which is low due to the small focal length, an optimization routine was run, which included the numerical calculations of the directivity for the whole structure. A small number of Fresnel zones $i = 7$ was found to be optimal. The calculated radius of the last zone was $r_7 = 12.5$ mm. The final lens had a total thickness of $5t_d + 4w = 1.973$ mm ($\sim 0.62\lambda_0$). Thus, the whole structure had dimensions of 32 mm × 32 mm × 1.973 mm. The final lens profile and fabricated Soret fishnet metalens is shown in Fig. 3.14(a,b).

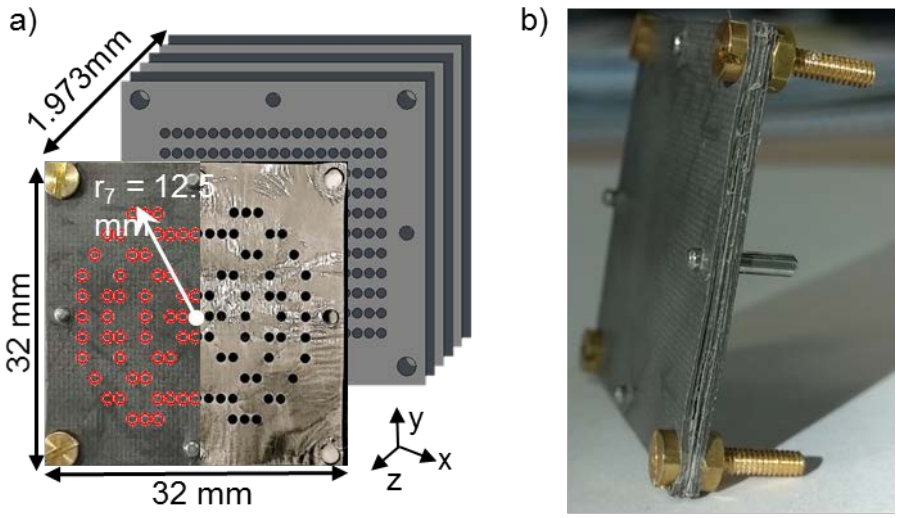

Fig. 3.14. Fabricated Soret fishnet metamaterial lens (a) front-view and its design with seven Fresnel zones. Light grey slabs account for perforated plates and dark grey for RO5880™ slabs; (b) side-view with alignment pins and fastening screws.

Fabrication.

The Soret fishnet lens was fabricated using aluminum foil with thickness 0.021±0.003 mm perforated and cut by laser (see Fig. 3.14). The substrate Rogers RO5880™ with permittivity $\varepsilon_r = 2.2$ and thickness 0.381 mm was used as dielectric spacer between successive aluminum foils and as additional protective outer layers. The pins were used to align the layers and screws to fasten all layers.

3.2.2 Analytical and simulation results

First, the power distribution was calculated as a function of frequency and position along the optical axis of the lens [Fig. 3.15(a)] using the Huygens-Fresnel principle. In this calculus, we model the holes as the point sources, who are located at the output plate. Also for simplicity we neglect reflection and absorption. Furthermore, all sources have the same amplitude and radiate vertically polarized (E_y) cylindrical waves. The absolute maximum in this case occurs at

95.5 GHz, with focal length FL_1 = 1.87 mm (~0.60λ_0). The secondary focus is located at FL_2 = 7.01 mm (~2.22λ_0) and has a significantly lower magnitude. As shown in Fig. 3.15(a), the Soret lens suffers from chromatic aberration, i.e. the focal point is shifted in frequency. Next, the power distribution colour-maps calculated at the design frequency are presented in Fig. 3.16(a, b) for the *xz*- and *yz*-plane respectively. In both cut-planes, clear foci can be observed with transverse dimensions 0.36λ_0 and 0.5λ_0 for *xz*- and *yz*-plane respectively.

In the next step, a full-wave numerical analysis of the realistic 3D model of the Soret fishnet metalens was done using the transient solver of the commercial software CST Microwave Studio™. The metal aluminum layer was modelled as a lossy metal with the bulk conductivity of aluminum ($\sigma_{Al} = 3.56\times10^7$ S/m). A fine hexahedral mesh was used with minimum and maximum mesh cell sizes of 0.088 mm (~0.03λ_0) and 0.25 mm (~0.08λ_0), respectively. The metalens was illuminated by a vertically polarized (E_y) plane wave impinging normally on the fishnet side. Perfectly matched layers (i.e., the solver-defined *open add space* boundaries) were used at the boundaries of the simulation box to emulate a lens in free space. Given the two-fold symmetry of the problem, electric and magnetic symmetries were imposed in the *xz*-plane (y = 0) and *yz*-plane (x = 0), respectively, to reduce computation time. The simulation was run for a sufficiently long time to ensure steady-state regime so that the continuous-wave information computed by Fourier transformations was valid. The colour-map of the power spectrum as a function of z position was obtained by placing E-field and H-field probes along the optical axis (*z*-axis) with a 0.05 mm step. These probes record the waveform at their positions and by Fourier transformation, the E- and H-field spectra are obtained. These full-wave numerical results should provide a better modelling of the lens than the analytical results, where some simplifications were made.

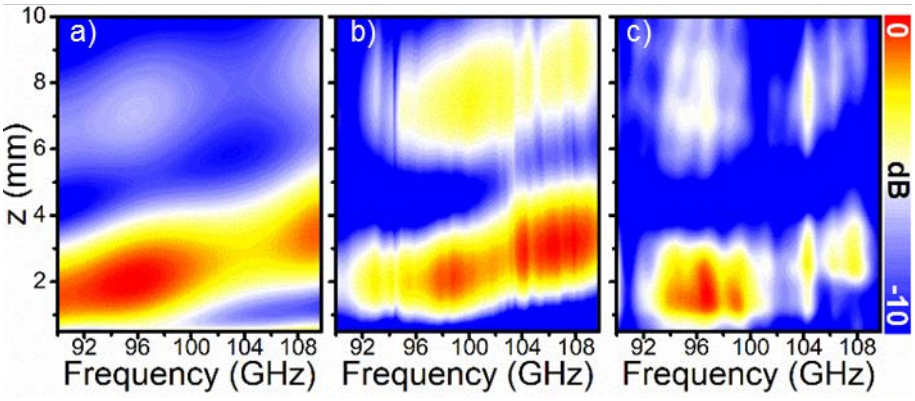

Fig. 3.15. Power spectra along the optical axis. Power distribution along *z* axis for the frequency range 90–110GHz: (a) analytical results, (b) simulation and (c) experimental results.

Initially, the power distribution as a function of frequency and position along the optical axis (*z*-axis) was obtained and is shown in Fig. 3.15(b). A focal spot appears within the frequency range 97-110 GHz, moving from 1.9 mm (0.57λ_0) up to 3 mm (0.95λ_0) along the *z*-axis. One can see that these results resemble closely the analytical results previously shown, but here the secondary focal spot is more prominent. The power enhancement (i.e., the ratio between the

intensity with and without lens for each *xz* position) corresponding to the first maximum is 10.28 dB at 98.75 GHz ($\lambda_0 \sim 3.04$ mm) with a focal distance $FL = 1.94$ mm ($\sim 0.64\lambda_0$).

Finally, the colour-map of power distribution was generated for *xz*- and *yz*-planes at 98.75 GHz (Fig. 3.16(c,d)). These colour-maps resemble the analytical results but again show minor dissimilarities because of the different accuracy of each method. The blueshift of the focal spot can be simply explained however by taking into account that in the analytical calculations we neglect the dielectric substrate covering the first layer that changes the effective permittivity at the output surface.

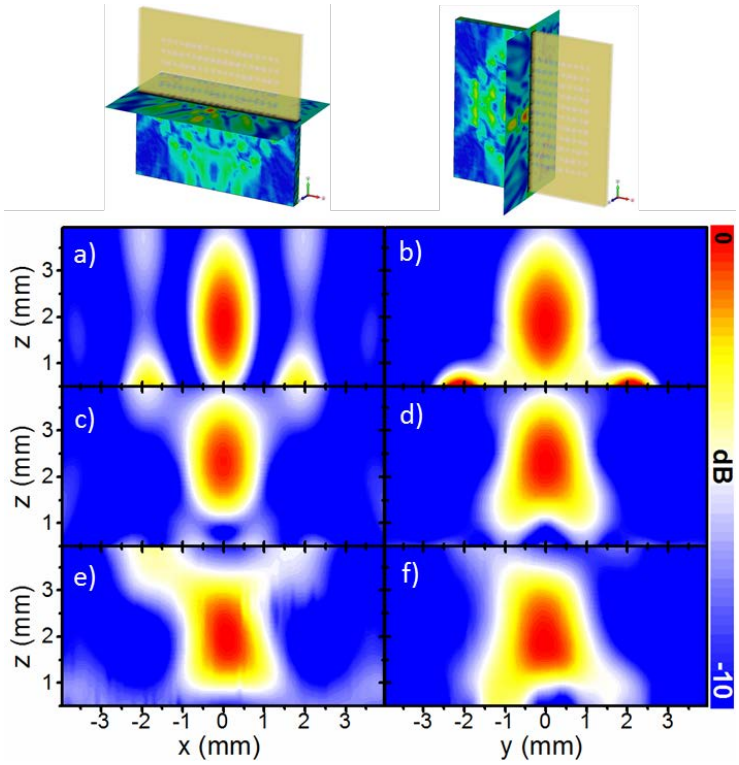

Fig. 3.16. Normalized spatial power distribution on the *xz*-plane (left column) and *yz*-plane (right column) for: (a-b) analytical results at 95.5 GHz; (c-d) simulation results at 96.45 GHz; (e-f) experimental results at 98.75 GHz. In inset representation of cutting plane in each case: *xz*-plane (left column) and *yz*-plane (right column).

3.2.3 Experimental results

The experimental verification was done using an AB MillimetreTM quasi-optical vector network analyzer with the setup illustrated in Fig 3.17. To illuminate the lens, a W-band corrugated horn antenna was placed at a distance $L = 4000$ mm from the lens. At this distance the radius beam waist of the Gaussian beam is ~400 mm, which ensures a uniform illumination of the lens. A waveguide probe WR-8.0 was used as a detector, for the *xz* raster scanning. Millimeter-wave absorbers were used throughout the setup to mimic anechoic chamber conditions.

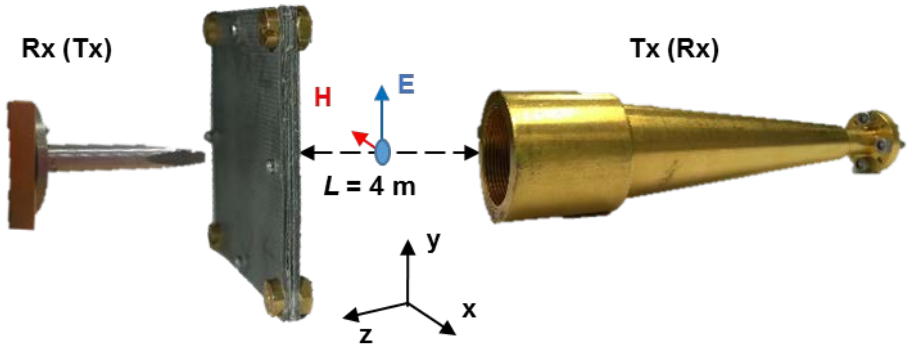

Fig. 3.17. Experimental setup. Scheme of experimental setup for the focus measurements (radiation measurements) with a waveguide probe as a receiver (transmitter) and a standard high gain horn antenna as a transmitter (receiver).

The calibration was done by recording the transmitted power without the lens. To obtain the power distribution as a function of frequency and *z* position, the lens was placed in the setup and the detector was moved from 0.5 to 10 mm away from the lens along *z*-axis (with 0.05 mm steps) while recording the spectrum in the range 90-110 GHz. The results are shown in Fig. 3.15(c) and confirm our preliminary analytical and numerical results. The maximum power enhancement is 11.04 dB at 96.45 GHz ($\lambda_0 \sim 3.11$ mm) with a focal distance $FL_1 = 1.9$ mm ($\sim 0.61\lambda_0$). A secondary focus appears at $FL_2 = 7$ mm ($2.25\lambda_0$) similarly to the analytical and numerical results. One can notice that for the experimental results the power enhancement is significantly lower within the frequency range 100-104 GHz. This can be due to the presence of thin air gaps between metallic and dielectric plates arising from imperfections of the fabrication. Additional simulations for the unit cell of the fishnet metamaterial were run and showed that indeed the air gaps inside the fishnet metamaterial deprecate its electromagnetic performance, reducing the transmitted power in this frequency range.

Next, the power was scanned on *xz*- and *yz*- planes at 96.45 GHz. The results of the spatial power distribution are shown in Fig. 3.16(e,f). The qualitative agreement with the numerical results is evident. To facilitate the comparison, all the results are gathered in Table II.

TABLE II.
FOCAL PROPERTIES AND RADIATION PATTERN PARAMETERS

	Frequency, GHz	***FL***[1], mm	***FWHM***[2], mm		***DF***[3], *mm*	**HPBW**[4], **deg**		**FNBW**[5], **deg**		**FSLL**[6], **deg**		**Directivity, dBi**
		E-plane *H*-plane	*E*-plane	*H*-plane	*E*-plane *H*-plane	*E*-plane	*H*-plane	*E*-plane	*H*-plane	*E*-plane	*H*-plane	
Analytical	95 $\lambda_0 = 3.15$ mm	1.87 $0.59\lambda_0$	1.13 $0.36\lambda_0$	1.58 $0.5\lambda_0$	1.45 $0.46\lambda_0$	-	-	-	-	-	-	-
Simulation	98.75 $\lambda_0 = 3.04$ mm	1.94 $0.64\lambda_0$	1.39 $0.46\lambda_0$	1.58 $0.52\lambda_0$	1.97 $0.65\lambda_0$	8.1	12.7	48	50	-13.1	-9.9	15.1
Experimenta	96.45 $\lambda_0 = 3.15$ mm	1.9 $0.61\lambda_0$	1.44 $0.46\lambda_0$	1.73 $0.56\lambda_0$	2 $0.64\lambda_0$	18.1	13.7	42	67	-13.5	-20.7	15.4

[1]FL is the focal length.
[2]FWHM is the full width at half maximum.
[3]DF is the depth of focus.
[4]HPBW is the half-power beam width
[5]FNBW is the first null beam width
[6]FSLL is the first side-lobe level

3.2.4 Metalens antenna.

After a characterization of the focal properties of the Soret fishnet metalens, next we investigate its performance as FZPA. To this end, the waveguide probe WR-8.0 was used as a feeder placed at the experimental focal length FL = 1.9 mm ($0.63\lambda_0$). A schematic of the experimental setup along with the fabricated Soret fishnet metamaterial lens is shown in Fig. 3.17. Notice that now the input part of the hybrid lens is the Soret lens and the output is composed of the fishnet metamaterial. Meanwhile, a high gain standard horn antenna was placed 4000 mm away from the flat face of the zoned lens to detect the radiated power. To measure the angular distribution of the radiated power, the feeder and the zoned lens stood on a rotating platform that can rotate from -90 deg to +90 deg with 0.5 deg step. Absorbing material was also used throughout the setup for reflection suppression. The normalized experimental results for co- and cross-polar components as a function of frequency and angle are shown in Fig. 3.18(e-f) *E*-plane and Fig. 3.18(g-h) *H*-plane.

In the numerical simulations the realized gain was directly calculated by the built-in far-field monitors of CST Microwave Studio™. The realistic waveguide probe WR-8.0 was used as a feeder and placed at the previously numerically-found position z = 1.9 mm, which corresponds to the maximum radiation of the FZPA. The rest of the simulation parameters were described previously. Far-field monitors were used to record the radiation pattern of the lens within the frequency range 90-110 GHz with a step of 0.25 GHz. Numerical results of co- and cross-polar angular power distributions for *E*- and *H*-plane are displayed in Fig. 3.18(a-d). The maximum is located at 98.75 GHz, in agreement with the previous numerical study. It is evident from these figures that the angular beamwidth for *H*-plane is wider than for *E*-plane. This can be explained by the excitation of leaky waves on the surface of the Soret lens, where the current density is higher and runs parallel to the *E*-plane [67], [68].

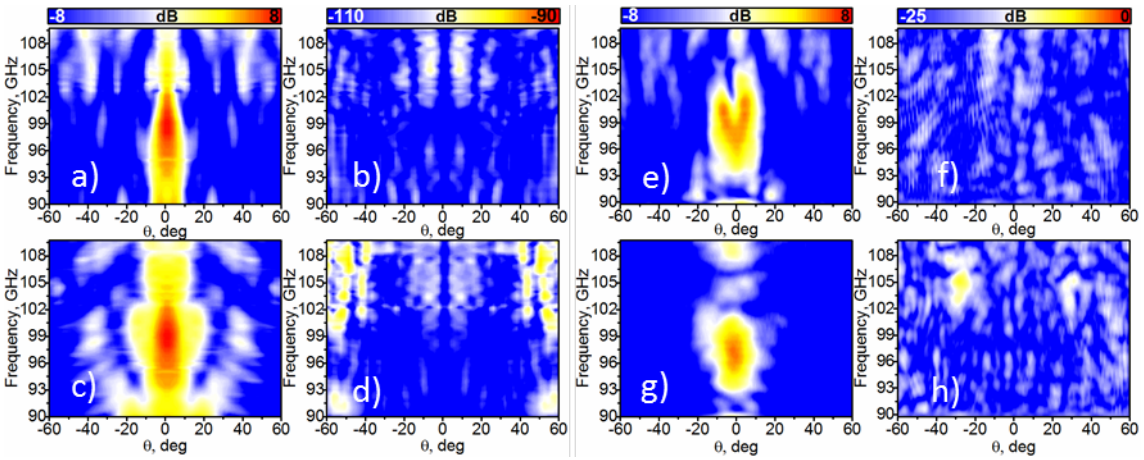

Fig. 3.18. Radiation pattern vs. frequency. The numerical (a-d) experimental (e-h) radiation pattern of the Soret fishnet metamaterial lens antenna in the frequency range 90-110 GHz: co- (a, c, e, g) and cross-polarization (b, d, f, h). (a, b ,e, f) E-plane and (c, d, g, h) H-plane.

One can notice the small disagreement between experimental and numerical results for the co-polar component for *E*-plane, in particular the division of the main beam for frequencies

99 – 103 GHz. Even though the experiment was done with the greatest possible care and precision, this could be well explained by an undesired tilt of the lens in the experimental setup since additional simulations for a tilted lens (with a tilt angle θ = 7 deg in *H*-plane) were run and demonstrated a similar pattern (not shown here). Consistently with the previous experiment (investigating the focal properties of the Soret lens) the experimental maximum is located at 96.45 GHz, i.e. slightly shifted from the frequency obtained by simulation. In Fig. 3.19(a, b), we plot together numerical and experimental results of the maximum at each respective frequency. In this figure, to facilitate the comparison, the normalized simulation and experimental radiation patterns for the *E*- and *H*-plane are presented. Logically, the performance is different, and most notably the beamwidth is wider in the experiment. Additional simulations prove that the frequency shift of 2 GHz provokes broadening of the beamwidth from 8.7 deg up to 13 deg. Another factor for the wider beamwidth in the experimental *E*-plane is a displacement of the waveguide probe. For example, in our case the focal displacement of 0.3 mm in the simulations increases the beamwidth from 8.7 deg up to 11 deg. The combination of these two factors widens the beam more than two times: from 8.7 deg up to 18.5 deg.

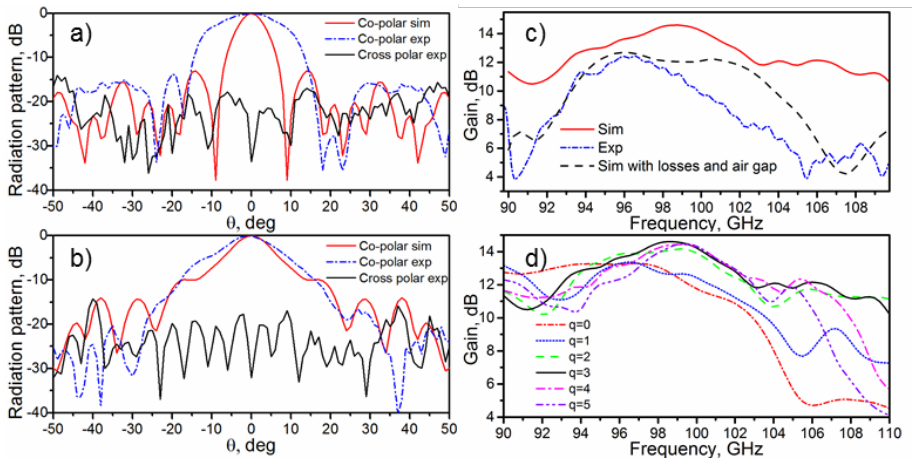

Fig. 3.19. Normalized radiation pattern and gain. Normalized radiation patterns for: (a) E-plane and (b) H-plane at frequencies 98.75 GHz 96.45 GHz (simulation and experimental respectively). (c) Simulation gain (solid red line), experimental gain (dash dotted blue line) and simulation gain considering air gaps and losses (dashed black line). (d) Simulation results for the gain of the Soret lens antenna with a different number of stacked plates *q*.

To complete the study, the numerical and experimental gain of the Soret fishnet metamaterial lens antenna is presented in Fig. 6(c). In the experiment, the gain was obtained by comparing our lens antenna with a standard horn antenna following the gain comparison method[69]. For this aim, the received power was measured using a standard gain horn antenna with the lens and waveguide probe as a transmitter. Then the lens was removed and a standard high gain horn antenna replaced the transmitter. As a result, high gain of 10.64 dB is found experimentally at 96.45 GHz (solid blue line). The numerical value of 14.6 dB is found at frequency 98.75 GHz by using the software-implemented far-field monitors (dashed red line). The difference in the results, the lower values of gain and shift in frequency, can be explained as

a sum of all previously described factors, such as experimental errors (misalignment, accuracy of distance measurement) and by defects in the fabrication (non-perfect contact between dielectric and metallic plates) and effective substrate losses higher than nominal values. To confirm these factors, additional simulations for the complete 3D model of the FZPA were run with an air gap of 50 μm and higher dielectric loss tangent tanδ = 0.015. The resulting gain is shown in Fig. 6(c) (dashed dotted black line). Here an air gap of 50 μm between metallic and dielectric plates results in a frequency shift of the maximum from 98.75 GHz to 96.25 GHz and the higher losses result in a lower gain. Consequently, the numerical gain of the lens with higher losses and spurious air gap is closer to the experimental gain. The maximum directivity, computed readily from the simulation, is 15.1 dBi at 98.75 GHz, and a directivity 15.4 dBi is estimated from experimental results at 96.45 GHz [60]. To facilitate the comparison, all the results are gathered in Table II.

In order to demonstrate the advantages and improvements of the hybrid Soret fishnet metamaterial lens antenna, we compare its performance in terms of gain for an increasing number of cascaded fishnet plates. As it was mentioned in the introduction, NZIM can improve the radiation parameters due to the redistribution of the energy on its boundaries. Since the phase advance inside NZIM is close to zero, at the output of the fishnet metamaterial the phase distribution is conformal to the exit surface, which is planar in our case. Therefore, the curved phase front, propagating from the Soret lens, is transformed into quasi-planar at the interface between the fishnet metamaterial and free space. Due to the inhomogeneity of the fishnet metamaterial, the NZIM regime depends on the number of the plates and tends to deviate significantly when this number is small. This can be clearly seen in Fig 3.20, where the E_y component on *yz*-plane at 98.75 GHz is plotted for a different number *q* of cascaded plates.

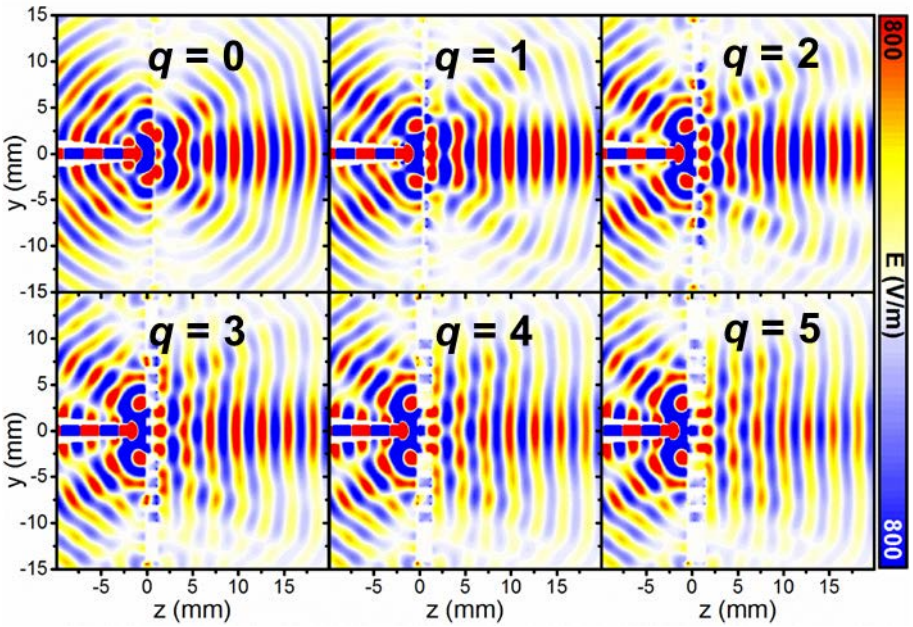

Fig. 3.20. Electric field distribution on the *yz*-plane. The colour-maps for the distribution of E_y component on the *yz*-plane for different number of stacked plates *q*.

With the increase of q, the field distribution at the output of the hybrid Soret fishnet metamaterial lens tends to become planar. As a result, the radiation is more directive, i.e. higher directivity and smaller side lobe level. In Fig. 3.19(d) the numerical results for the gain are shown for an increasing number of plates q = 0, 1, 2, 3, 4, 5 (q = 0 refers to the case when only the first layer of the lens sandwiched between substrate layers (RO5880^{TM}) is present).

From these figures, it is evident that increasing the number of plates improves the directivity of the hybrid Soret fishnet metamaterial lens. However, a large number results in an increased thickness and therefore higher losses. Hence, for q > 3, the gain decreases. As a compromise solution, we thus designed our lens with the first Soret layer plus 3 fishnet plates. Such design ensures lower losses and a maximum gain of metalens antenna.

4 Chapter IV. Carpet Cloaking

The ability to become invisible was primarily a subject of different tales and science fiction novels, in which heroes could hide from others by wearing a special cloak. However, recently thanks to the rapid progress of metamaterials, the path towards invisibility is gradually becoming possible. The topic is evolving fast and now is one of the most thrilling applications based on metamaterials. In this chapter we introduce a metasurface based carpet cloaking, which is able to conceal an object on a ground plane from the incident wave.

4.1 Carpet cloaking based on metasurface

In Chapter I we already disscussed metamaterials, which allow to tailor at will the intrinsic electromagnetic parameters of a composite, such as its permittivity and permeability, providing interesting solutions for one of the oldest quests of electromagnetism – controlling electromagnetic waves at will[4], [70]. The cloaking devices[9], [71]–[73], able to hide objects from an external observer, are some of the applications which also have greatly benefited from the appearance of metamaterials. After years of intensive studies, several cloaking mechanisms and designs have been proposed, mostly among the two leading categories of transformation optics[45], [46] and scattering cancelation[47], [48], [74]. The first technique based on transformation optics represents an idea to manipulate the electromagnetic flow using a transformation that stretches the coordinate grid of space, as showed in Fig.4.1.

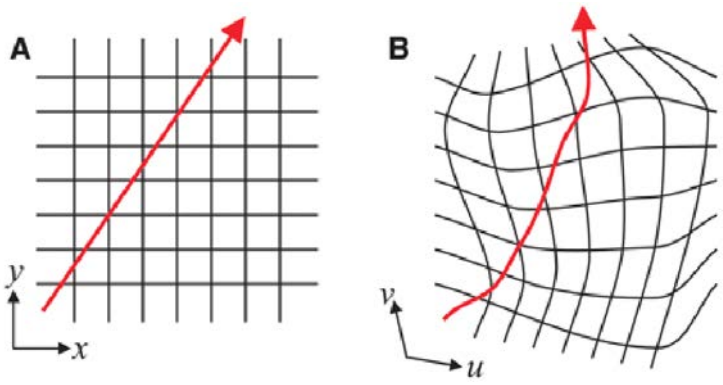

Fig. 4.1. Illustration of the ray distortion offered by transformation optics. ©2006 AAAS, [46].

However this technique imposes strong demands on bulk metamaterial designs, such as a specific profile of inhomogeneity and anisotropy of the material parameters. These constraints make such cloaking devices difficult to realize in practice, due to their high complexity. The cloaks based on the second principle – scattering cancellation – are simpler to realize and more robust[75], yet, like any passive cloaking technique, they suffer from fundamental limitations on the size of the object to be cloaked[76].

A cloaking approach that relaxes the causality limitations on size and bandwidth is known as carpet cloaking or ground cloaking, with the idea of hiding in reflection a bump on a mirror.

The principle of this type of cloak is shown in Fig. 4.2[77]. This problem has gained the interest of many researchers, due to its inherently relaxed constraints, its simplified design, and wide range of applications. Transformation-based carpet cloaks exploit quasi-conformal mapping[77], [78], which allows to minimize the anisotropy of the required material and can be implemented using isotropic dielectrics[79], simplifying the design and minimizing absorption losses.

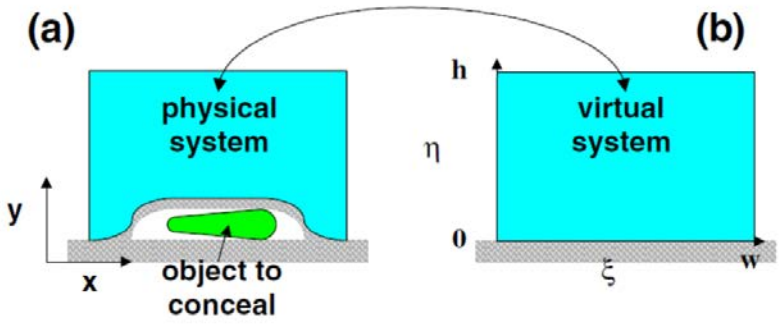

Fig. 4.2. Principle of operation of a carpet cloak. ©2008 APS, [77]

However, the proposed cloak is still volumetric and non-trivial to realize. Another important hurdle for practical applications of carpet cloaks is the lateral shift they introduce under the isotropic approximation. Unfortunately, the introduced lateral shift is comparable to the case when a ground plane is placed above the cloaked object to suppress its scattering. Since the cloaking medium is typically denser than free-space, the beam inside the cloak is refracted into a smaller angle. However, if we require that a finite-size beam emerges from the cloak at the same location as it would when reflected by a flat ground plane, it should be refracted into a larger angle, which is only possible in anisotropic materials. This lateral shift presents a serious problem, since an external observer still can notice that the beam emerges from a different point[80], and it also begs the question of whether another flat reflector on top of the bump would not provide a simpler solution to the problem. This problem is illustrated in Fig. 4.3[80].

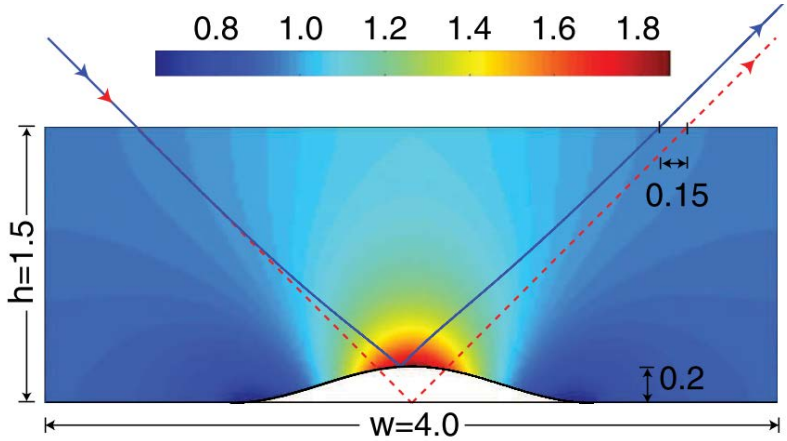

Fig. 4.3. A ray (blue solid line) incident at 45 deg with respect to the normal onto an isotropic ground-plane cloak. The red dotted line represents the trajectory of a ray reflecting on a flat ground plane. Notice the distorted ray has been shifted on top of the cloak toward the incident point. ©2010 APS, [80].

To overcome the issues associated with conventional ground cloaking approaches, recently it has been proposed that covering a bump with a specially designed surface can reduce unwanted scattering from an arbitrary bump, creating an effective ultrathin *cloaking surface*[81], [82]. The metasurface is used to build a phase distribution on the bump edge equal to the phase response created upon reflection from a conducting ground plane, i.e. when no bump is present. In this case, for the external observer the reflected wave will have the same phase distribution as if it were reflected from the ground plane, creating an ultrathin, and relatively simple cloaking configuration for practical implementation. Moreover, due to surface phase compensation, the metasurface cloak does not create a lateral shift[81]. Obviously this approach is dependent on the object to hide and the illumination, but, given its robustness, it may provide a viable solution for several practical applications.

Carpet cloak design

Fig. 4.4 shows the general scheme of the cloak and of the object. The incoming oblique wave, with angle of incidence θ (with respect to the horizontal ground plane), illuminates a PEC bump with a tilt angle ψ. Any arbitrary object we aim to conceal can be placed inside the bump, as long as it fits in its volume. The goal is to create a field distribution on the external boundary of the object (dashed line), identical to the case when no bump is presented, in view of the field equivalence principle. This technique is different from carpet cloaks based on the quasi-conformal mapping, where the object is concealed by controlling the propagation of the incident waves and effectively isolating the hidden region from the incident wave. Here, reconstruction of the field can be done by introducing an abrupt phase variation on the boundary, which can be calculated at each point of the bump's edge as:

$$\delta = \pi - 2k_0 h\cos\theta\,, \tag{4.1}$$

where k_0 is the free space wave vector at the operation frequency, h is the height of the unit cell center from the ground plane, and θ is the angle of incidence of the incoming wave with respect to the back-plane normal.

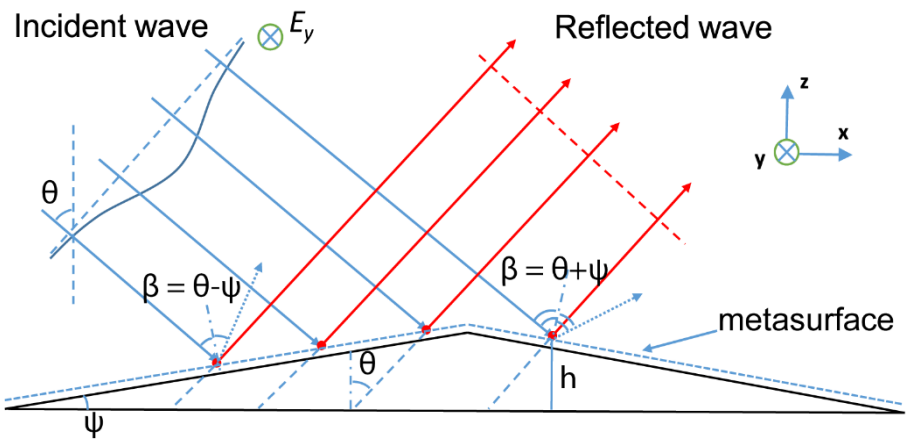

Fig. 4.4. Scheme of the carpet cloak with metasurface.

4.2 Simulation results

4.2.1 Cloaking metasurface

In order to obtain the required phase distribution, a metasurface based on pairs of closed ring resonators (CRR) is employed, whose unit cell is shown in the inset of Fig. 4.5(a). A clear advantage of such topology is its insensitivity to the polarization of the incident electromagnetic field. To realize the effect, we need to be able to control the phase response of the reflected wave from each block over the entire 2π phase range. To this purpose, we simulated the reflection from infinite planar arrays of such closed rings using the commercial software CST Microwave Studio^{TM}[53], using unit cell boundaries and frequency-domain solver. A fine tetrahedral mesh was chosen with maximum edge length 0.285 mm ($0.076\lambda_0$) and minimum edge length 0.0007 mm ($0.0002\lambda_0$). To create a high resolution surface with better control over the phase distribution of the reflected beam, the lateral dimension of the unit cell was fixed at 400 um $\approx \lambda_0/10$, for the working frequency f = 80 GHz (λ_0 = 3.750 mm). Each unit cell consists of two concentric metallic rings with a fixed width w = 10 um, separated by a gap g = 10 um. The radius of the outer ring is then found as $r_2 = r_1+w+g$, where r_1 is the radius of the inner ring. The rings are separated from the ground plane by a thin silicon layer of thickness h = 165 um ($\approx \lambda_0/22$) with dielectric permittivity $\varepsilon_r = 11.2$ and loss tangent $\tan\delta = 4.7\times10^{-6}$. The metal used for the rings is aluminum with a conductivity $\sigma_{Al} = 3.56\times10^7$ S/m.

Due to the geometry of the carpet cloak, the incoming wave has two possible incidence angles (β) on each block of the metasurface, depending on which side of the bump the block is located. In our particular case for an obliquely incident wave with angle $\theta = 45°$ and tilt angle of the bump $\psi = 20°$, the incidence angles at the bump edges are $\beta_1 = \theta - \psi = 25°$ and $\beta_2 = \theta + \psi = 65°$ for the left and right side respectively. The amplitude and phase of the reflection coefficient was obtained as a function of the radius of the inner ring and the angle of incidence β, shown in Fig. 4.5 (b-c). In order to increase the design precision, instead of the normal reflection coefficients, here we design the cloaking layers on each side of the bump based on the data calculated for the corresponding incidence angles. As observed in Fig. 4.5(a- b), the amplitude of the reflected beam slightly drops around r_1 =135 um, due to the CRR resonance. Apart from the resonance, however, the metasurface is operating almost as an ideal mirror with close to unitary efficiency. Fig. 4.5(a) also shows the phase response of the unit cell for two incidence angles β_1 (solid blue line) and β_2 (dash dotted blue line). The range of phase variation changing the inclusion radius spans almost 2π, confirming that this unit cell can adequately control the local phase response of the cloaking metasurface. It is also clearly seen that for a larger incidence angle the phase response has a steeper slope and, therefore, it is more sensitive to the radius variation of the rings, as it may be expected. This means that a bump with a larger tilt angle requires a metasurface with a smaller variation of radii, in the order of a few μm.

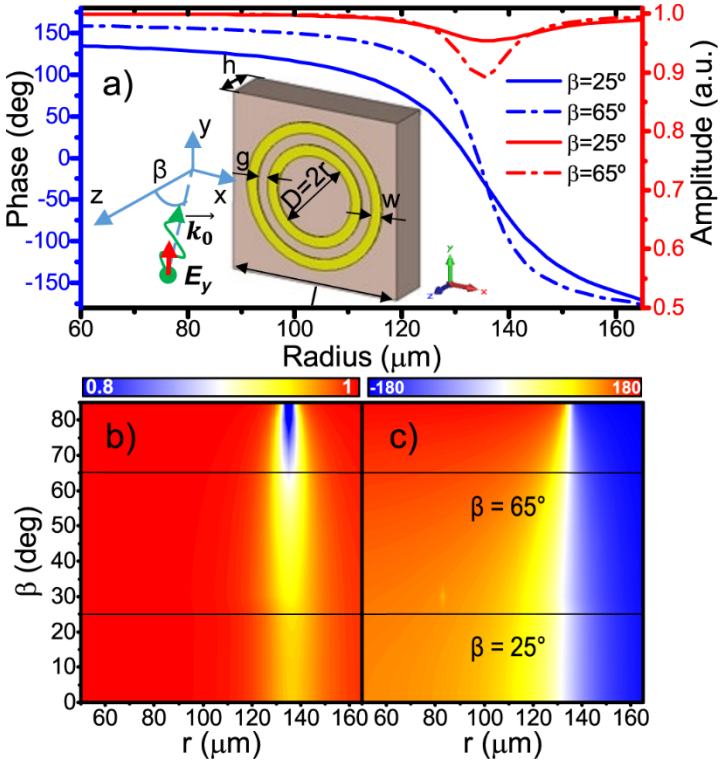

Fig. 4.5. (a) Phase response of the unit cell for different angles of incidence. (Inset indicates the unit cell geometry and its corresponding parameters.) Color-map for the amplitude (b) and phase (c) of the reflection coefficient as a function of the incidence angle and radius of the inner ring.

4.2.2 Carpet cloak performance

Once the phase response of the unit cell has been characterized, it is possible to put together the carpet cloak using the design equation (4.1), in order to hide a perfectly conducting bump with triangular shape laying in the *xz*-plane and infinite in the transverse *y* direction. For practical realizations, it is preferred to cloak electrically large objects with bigger tilt angles, which allows to more efficiently utilize the space under the cloak. Extreme shapes and large corner angles may require nonlocal and active surfaces[83], but for slowly varying configurations, including the current proposed design, surface phase engineering is adequate[81]. The ground cloak was designed for a bump with a tilt angle $\psi = 20°$, height of 4.09 mm ($1.09\lambda_0$), edge length of 12 mm ($3.2\lambda_0$) and base length 22.55 mm ($6.01\lambda_0$). Full-wave simulations of the structure were performed using the transient solver CST Microwave Studio™. The structure was illuminated by an obliquely incident ($\theta = 45°$) Gaussian beam with *TE* polarization. To this end, an array of electric dipoles was used with Gaussian distribution of amplitudes, providing a quasi-Gaussian beam excitation. The ground plane was emulated by using an electric boundary (perfect electric conductor) in the *xy*-plane ($z = 0$). Given the symmetry of the structure an electric symmetry was applied in the *xz*-plane ($y = l/2$) in order to reduce computational time. A fine hexahedral mesh was applied with minimum cell length of 0.1 mm ($0.026\lambda_0$) and maximum of 0.44 mm ($0.112\lambda_0$)

As explained above, the phase response of the each block was obtained using unit cell boundaries, assuming that all cells in each simulation have the same parameters. On the contrary, to successfully mimic the ground plane, the radii of the rings must change according to the phase distribution determined by (4.1). The transverse inhomogeneities modify the mutual coupling between adjacent blocks, and therefore, its response to the incident wave. Hence, an optimization procedure is required to fine tune the design based on (4.1), imparting a local variation to the radii of surface blocks (60 blocks in the current design). Due to the reciprocity principle[84], we need to optimize only half of the bump, so only 30 unit cells need to be considered in the optimization process.

Fig. 4.6(a-c) show the spatial distribution of electric field (E_y component) at the operation frequency f_0 = 80 GHz for three cases: (a) ground plane, (b) bare bump and (c) cloaked bump.

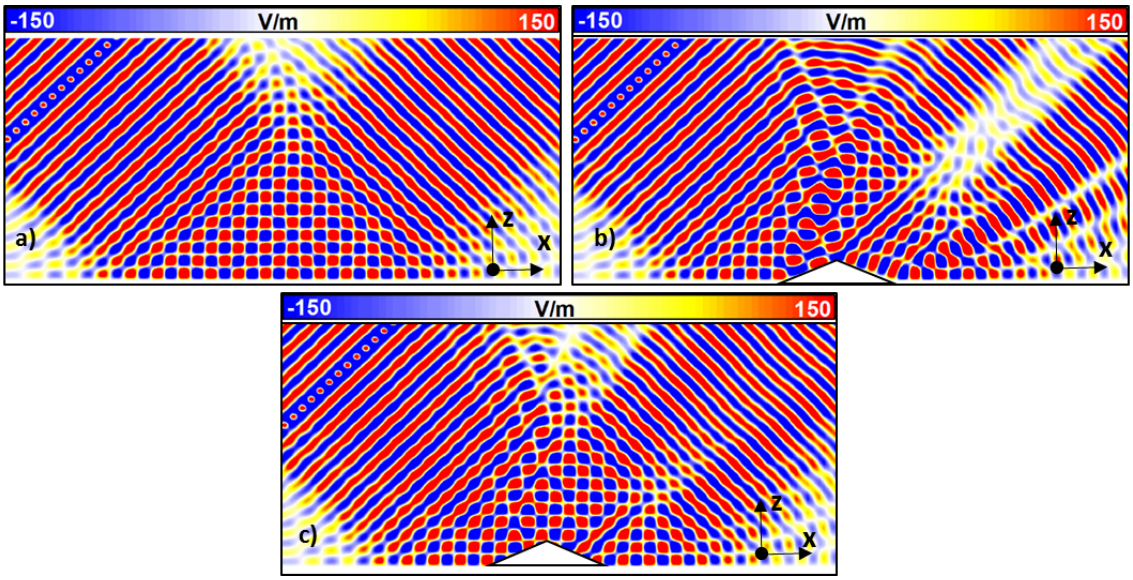

Fig. 4.6 Electric field distribution on *xz* plane for (a) ground plane, (b) bare bump, and (c) cloaked bump.

As it can be seen, when an irregularity is introduced on the ground plane the Gaussian beam is scattered over a wide a range of the angles. After the cloak is applied, the near-field distribution of the reflected wave is restored to the original Gaussian beam. The small disturbance of the reflected beam is caused by the finite discretization of the cloaking metasurface and high ($\beta = 65°$) incidence angle at the second edge of the bump, which may be mitigated with active cloaking surfaces[83]. As it was shown in Fig. 4.5(a) absorption losses are higher for high angles of incidence, provoking higher scattering level. Despite all these factors, Fig. 4.7 demonstrates that we are able to obtain a similar far-field radiation pattern from the cloaked beam as if a bare ground plane were interacting with the incident wave.

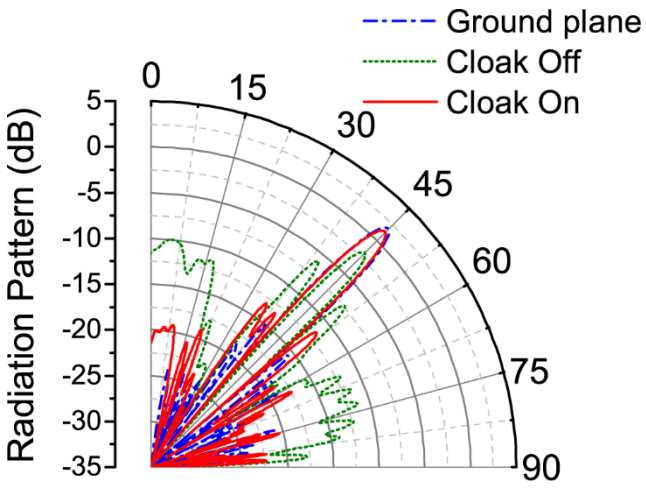

Fig. 4.7. Radiation pattern for the reflected Gaussian beam from the ground plane (dash-dotted blue line), the bump without cloak (dotted green line), and from the cloaked bump (solid red line).

4.2.3 Carpet cloak bandwidth

Next, the performance of the optimized cloak was analyzed in terms of the angle and frequency bandwidth. For this study, the numerical simulations were run within a frequency span from 75 to 85 GHz with a step of 0.2 GHz and steering the incidence angle from 25° to 60° with a step of 1°. The resulting color-maps for the far-field scattering electric field magnitude as a function of azimuth angle and frequency are shown in Fig. 4.8 (a-c). Analogous color-maps for the far-field magnitude as a function of azimuth angle and incident angle θ of the incoming wave are shown in Fig. 4.8 (d-f). The cloak works close to ideally at the designed frequency and angle of incidence, yet, and in spite of the original unidirectional design, it is able to significantly reduce the scattering level in the whole simulated range of frequencies and incidence angles. The multi-lobe pattern created in the presence of the bump is converted into a directive beam, as desired for an ideal ground plane.

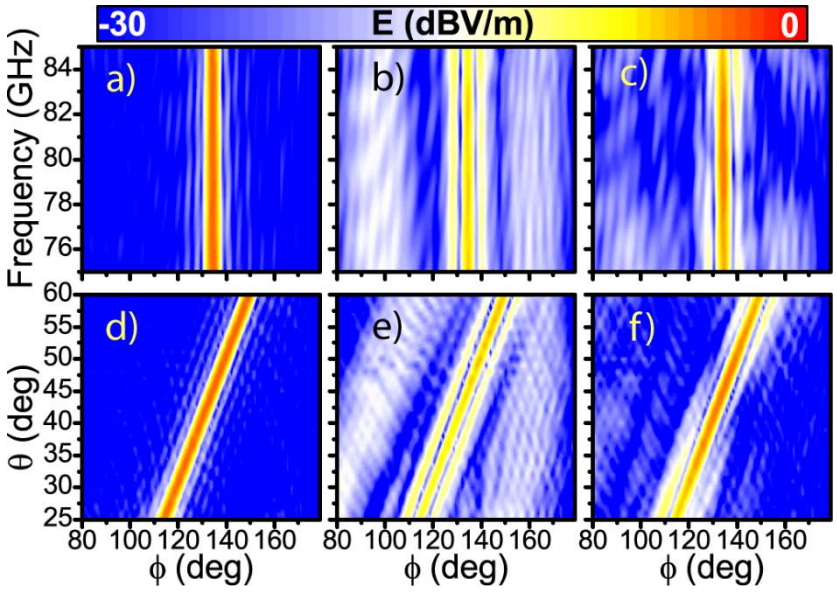

Fig. 4.8. Amplitude of the far-field component of the electric field as a function of azimuth angle ϕ and frequency (a)–(c) and as a function of the incidence angle θ and azimuth angle ϕ (d)–(f). Left column refers to the beam reflected from the ground plane, center from the bare bump, and right column from the bump covered with the cloak.

In order to quantitatively define the region over which the beam reconstruction is acceptable we use a root mean square error (RMSE), which determines the goodness of the fit, and can be defined as [85]:

$$RMSE(f,\theta)=\sqrt{\frac{1}{N}\sum_{i=1}^{N}\left[E_s(f,\theta,\phi_i)-E_b(f,\theta,\phi_i)\right]^2} \tag{4.2}$$

where N is the number of sample azimuth angles, $E_s(f, \theta, \varphi_i)$ and $E_b(f, \theta, \varphi_i)$ are the far-field magnitude of the reflected wave from the bump and the ground plane at given azimuth angle φ_i, frequency f, and incident angle θ. The calculated RMSE(f, θ) for the scattered beam without and with the cloak are shown in Figs. 4.9(a) and (b). A sufficiently accurate fit is considered for the RMSE less than 10% [86]. Hence, our parametric study reveals that the ground cloak maintains a reasonable performance in a frequency span of about 8 GHz (fractional bandwidth FBW = 10%) and angular span of 35°. In addition, it is noticeable that the cloak has a wider bandwidth for the lower incident angles, which is in good agreement with our previous study for the phase response as a function of the incident angle β. For applications in which the accuracy of the recovered beam is important, for example for high precision measurements, an RMSE below 5% (dash contour line in Fig. 4.9(c)) would still provide a bandwidth of 2.2 GHz (FBW = 3%) and angular span of 10°.

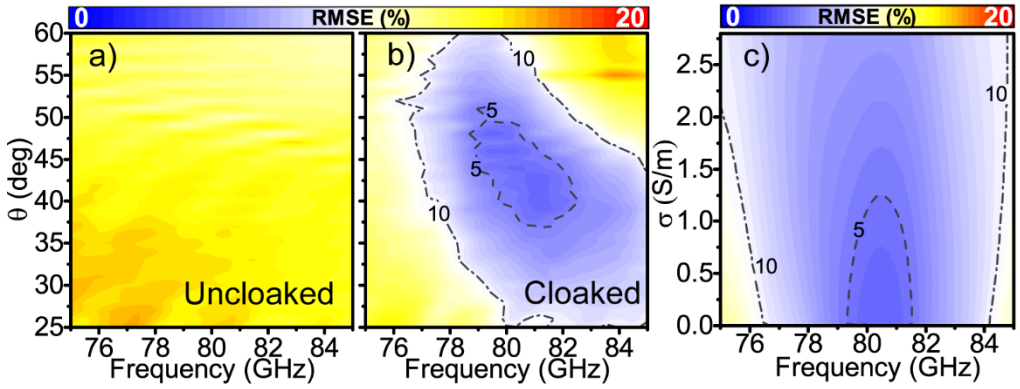

Fig. 4.9. RMSE distribution vs incident angle and frequency for (a) uncloaked and (b) cloaked bump. (c) RMSE distribution as a function of the conductivity σ of dielectric substrate and frequency.

These results have been obtained for relatively small substrate losses ($\tan\delta = 4.7\times10^{-6}$ or $\sigma = 2.5\times10^{-4}$ S/m). However, in practical realizations the losses can be several orders higher and may disrupt the cloak operation. Therefore, an analysis of the performance of the cloak was done for higher values of dielectric losses. The recovery of the Gaussian beam at the operational

frequency 80 GHz was estimated for different values of conductivity, using the same RMSE metric, and corresponding results are plotted in Fig. 4.9(c). Interestingly, even for very low RMSE (<5%) the cloaking metasurface is able to recover the far-field pattern of the original reflected Gaussian beam for values of conductivity up to 1.2 S/m ($\tan\delta = 0.023$), as it may be expected due to the inherently nonresonant nature of the proposed cloaking technique. Silicon samples with an equivalent value of resistivity $\rho = 83\ \Omega\cdot$cm are relatively cheap and commercially available, making the proposed cloaking device appealing for low cost THz devices such as automotive radar systems, to reduce unwanted scattering from electrically large objects .

The proposed cloaking metasurface is polarization insensitive and has a simple geometry, which facilitates the fabrication and reduces cost. Moreover, the proposed cloak demonstrates an acceptable beam reconstruction over a good angular span of 35° and a moderately broad bandwidth FBW = 10%. Such cloak can conceal electrically large objects and may find applications in radar and antenna systems, where other techniques may not be as practical due to their excessively large volumes.

5 Chapter V. Conclusions and Future Work

In this chapter, a summary of the conclusions obtained throughout this work is presented. In addition, we propose a list of future lines emerging from the work done and that could be studied in the future.

5.1 Conclusions

- The analysis shown so far demonstrates that strong dispersion of the fishnet, usually considered as a drawback, can be turned into an advantage to design broadband diffractive optical devices. Additionally, the narrow band of the fishnet guarantees the filtering of the undesired frequencies, whereas the strong dispersion allows designing the lens with more than one narrow working frequency with different focal lengths suitable for non-mechanical zooming.

- The basic aspects of designing a dual-band zoned fishnet metamaterial lens have been discussed. The strong dispersion of the fishnet, that otherwise would be a handicap, is here shown to be an advantage when combined with the zoning technique.

- The low-profile and weight of the zoned lens together with its ability to operate in two nearby narrow bands with good free-space matching make it a good competitor to other diffractive optical devices made of dielectrics (which tend to be lossy and mismatched for millimeter and submillimeter-waves) or metals (which tend to be mismatched).

- The converging broadband zoned fishnet metamaterial lens has been designed, fabricated and measured at the V-band of the millimeter-waves. Numerical results demonstrate a broadband regime with maximum enhancement of 11.2 dB and fractional bandwidth of 8.5%, which is almost 3 times wider than the previous single-band zoned fishnet metamaterial lens. Experimentally the performance of the zoned lens was demonstrated at f_1 = 54 GHz and f_2 = 55.5 GHz, showing good agreement with analytical and simulation results.

- A lens antenna has been subsequently proposed. The numerical results have been confirmed experimentally showing directivities above 15 dB for both frequency bands.

- A Soret metalens based on fishnet metamaterial has been designed, fabricated and analyzed. The basic aspect of Fresnel zone plate design has been discussed. Analytical and numerical results show good performance and agreement with designed parameters.

- The fabricated lens has been experimentally verified. The experimental results show the good performance of the lens and agreement with analytical and simulation results. The subwavelength transverse resolution (0.6λ) of the focal spot has been confirmed, with maximum enhancement of 11.04 dB at f = 96.45 GHz.

- Consequently, the hybrid Soret fishnet metamaterial lens antenna has been measured at millimetre-waves. The analysis demonstrated that the application of the metamaterial with a refractive index near zero could improve the radiation characteristics.

- It was demonstrated that, due to the inhomogeneity of the fishnet metamaterial, an optimum number of three stacked fishnet plates is required.

- The lens antenna configuration, which is thin, relatively cheap and easy to fabricate, demonstrates a solution to improve the radiation characteristics of the FZPAs. Such compact devices can find applications in wireless systems.

- It was shown that a metasurface based on array of closed ring resonators allows to manipulate the phase of reflected wave in almost 2π range.

- The carpet cloak based on this metasurface has been designed and numerically analyzed at 80 GHz. It was shown that the cloak could successfully conceal an electrically large object (1.1λ) from the impinging wave.

- It was shown that designed cloak is relatively robust to angle and frequency sweep. The cloak works for angle span of 35° and has fractional bandwidth of 10%.

5.2 Future work

- Study of improved Soret lens, so called Wood zoned plate. The principal difference is to replace the opaque rings (negative or even zones) with transparent rings, which transmit a wave with π shift (λ/2) in order to create constructive interference. In this case, the even zones could be implemented with different hole array, which has unit cell with different period or radius of the hole.

- Fabrication of the proposed carpet cloak and its experimental demonstration at 80 GHz.

- Study of carpet cloak based on metasurface with subwavelength grating. In this case, the metasurface with subwavelength grating can create a required phase variation of reflected circular polarization, using a Pancharatnam-Berry phase principle. This phase is based on the anisotropic effective permittivity of the subwavelength grating and depends on the

direction of the grating vector. By rotating the grating vector, it is possible to change the reflected phase of the circular polarization in 2π range.

- Study of possibility to use a graphene or a graphene-dielectric metamaterial as a cloaking metasurface in carpet cloaking. The graphene is a one-atom thick carbon layer that can change its surface impedance with variation of its chemical potential. This gives a possibility to manipulate with reflected phase.

6 Appendix A

6.1 Matlab Code for carpet cloaking optimization

```
clearvars -except t_group t_mws t_cst t_solid t_solver folder
c=300; f=80;   d=.400; l=c/f; k0=2*pi/l; theta=45; p= [0 20 0];
psi=p(2)*pi/180;    b=theta.*pi/180;    dx=d*cos(psi);
tm=.002;    ts=.2;  w=.01; k=.01; dy=d;
mat='Silicon (lossy)';
i=1;
x1=ts/sin(psi); xsi1=ts*cos(psi)*cot(psi);
dh=ts/cos(psi); pr=3.;  x=xsi1+dx/2:dx:pr*l; delx=ts*sin(psi);
L=(x(end)+dx/2+delx)*2;
hmax=L/2*tan(psi);
xi= [xsi1+dx/2:dx:L/2-dx/2-delx, L/2+delx+dx/2:dx:L-dx/2-xsi1];
xm=find(xi>L/2,1,'first');xs=d/2+ts/tan(psi):d:length(xi)*d-d/2-ts/tan(psi);
for i=1:length(xi)
    if i<xm
        h(i)=xi(i)*tan(psi);
    else
        h(i)=(L-xi(i))*tan(psi);
    end
end
for i=1:length(xi)
    phit(i)=pi-2*k0*h(i)*cos(b);
end

for i=1:length(phit);
phitwr(i)=rem(phit(i),2*pi);
     if phitwr(i)>pi
        phitwr(i)=phitwr(i)-2*pi;
     elseif phitwr(i)<-pi
        phitwr(i)=phitwr(i)+2*pi;
    end
end
phitwr=phitwr.*180./pi;
ratio=hmax/l
% profile approximation
clear phi phase ph fr
load('C:\Users\Baha\OneDrive\results\SRR\2rings\theta=35_80GHz_r_sweep_sil_l=300_ts=165_w=10_k=10.mat
','par','x','y')
fr=f;fi=find(x>=fr,1,'first');
r2=par./1000;
par=r2-k-w;
ph(:,:)=y(:,fi);
phase=ph(:,1);
% phase=fase;
for ii=1:xm-1
     [c ind(ii)]=min(abs(phase(:)-phitwr(ii)));
    phis(ii)=phase(ind(ii));
    r1(ii)=par(ind(ii));
    phis(length(xi)-ii+1)=phase(ind(ii));
    r1(length(xi)-ii+1)=par(ind(ii));

end
ks(1:length(xi))=k;
r2=r1+k+w;
plot(xi,phis,xi,phitwr)

%% Prepare simuation
t_cst = actxserver('CSTStudio.application');
t_mws = invoke(t_cst, 'NewMWS') ;
setappdata(0,'mws',t_mws);
filename='G:\Simulaciones\CST\cloaking\with
rings\Optimization\010315_ground_cloak_optim_57GHz_big_real.cst';
invoke(t_mws, 'OpenFile', filename);
%%
t_solid=invoke(t_mws,'Solid');
t_group=invoke(t_mws,'Group');
t_solver = invoke(t_mws, 'Solver');
t_treeitem='Tables\1D Results\slope_e-field (f=f) (gauss_1)';
t_treeitem2='Tables\1D Results\slope_e-field (f=f) (gauss_1)_1_unwrapped';
t_ffitem='Farfields\farfield (f=f)  [gauss_1]';
t_name_phase= [folder 'phase.txt'];
t_name_mag= [folder 'mag.txt'];
t_name_ff= [folder 'ff.txt'];
%% Update structure
nport=21;
dport=2.5;
```

```
s=25;
sigma=.001;
R=50;
    b=theta*pi/180;
    xport=0.7*L-R*sin(b)-(nport*dport*cos(b))/2;
    zport=R*cos(b)-(nport*dport*sin(b))/2;
invoke(t_mws, 'StoreParameter','upperx', 25);
invoke(t_mws, 'StoreParameter','upperz', 3);
invoke(t_mws, 'StoreParameter','lowerx', 3);
invoke(t_mws, 'StoreParameter','lowerz', 0);
invoke(t_mws, 'StoreParameter','l', L);
invoke(t_mws, 'StoreParameter','psi', p(2));
invoke(t_mws, 'StoreParameter','dy', dy);
invoke(t_mws, 'StoreParameter','theta', theta);
invoke(t_mws, 'StoreParameter','tsub', ts);
invoke(t_mws, 'StoreParameter','h', hmax);
invoke(t_mws, 'StoreParameter','x1', x1);
invoke(t_mws, 'StoreParameter','dh', dh);
invoke(t_mws, 'StoreParameter','f', fr);
invoke(t_mws, 'StoreParameter','xport', xport);
invoke(t_mws, 'StoreParameter','zport', zport);
invoke(t_mws, 'StoreParameter','dport', dport);
invoke(t_mws, 'StoreParameter','sigma', sigma);
invoke(t_mws, 'Rebuild');

%% Base
clear amp ampb ampwc ang_ffb ang_ffn
invoke(t_solid,'ChangeMaterial','component1:hump',    'Vacuum')
invoke(t_solid,'ChangeMaterial','component1:substrate','Vacuum')
invoke(t_solver, 'Start');
invoke(t_mws,'SelectTreeItem','2D/3D Results\E-Field\e-field (f=f)  [gauss_1]\Y')
    invoke(t_mws,'Plot3DPlotsOn2DPlane','True')
    t_cstplot=invoke(t_mws,'ScalarPlot2D');
    invoke(t_cstplot,'PlaneNormal','y')
    invoke(t_cstplot,'PlaneCoordinate',dy/2)
    invoke(t_cstplot,'ScaleToRange','True')
    invoke(t_cstplot,'ScaleRange',-900,900)
    t_inname= ['Inicial_' date];
    invoke(t_mws,'StoreViewInClipboard')
    invoke(t_mws,'StoreViewInBmpFile', [pwd '\Ey_ground_' t_inname '.bmp'])
num=0;
ascii_exp(t_treeitem2,t_name_phase,'phase');
ascii_exp(t_treeitem,t_name_mag,'magnitude');
ascii_exp(t_ffitem,t_name_ff,'magnitude');
t_A = importdata(t_name_phase, ' ', 4);
t_B = importdata(t_name_mag, ' ', 4);
t_FF = importdata(t_name_ff, ' ', 4);
xfb(:,1) = t_A.data(:, 1);       % x-data column
faseb = t_A.data(:, 2);       % y-data column
ampb = t_B.data(:, 2);
fasebwr=unwrap(faseb,180);
ang_ffb=t_FF.data(:, 1);
mag_ffb=t_FF.data(:, 3);
%% Cloak off
invoke(t_mws, 'Rebuild');
invoke(t_solid,'ChangeMaterial','component1:hump','PEC')
invoke(t_solid,'ChangeMaterial','component1:substrate','Vacuum')
invoke(t_solver, 'Start');
invoke(t_mws,'SelectTreeItem','2D/3D Results\E-Field\e-field (f=f)  [gauss_1]\Y')
    invoke(t_mws,'Plot3DPlotsOn2DPlane','True')
    t_cstplot=invoke(t_mws,'ScalarPlot2D');
    invoke(t_cstplot,'PlaneNormal','y')
    invoke(t_cstplot,'PlaneCoordinate',dy/2)
    invoke(t_cstplot,'ScaleToRange','True')
    invoke(t_cstplot,'ScaleRange',-900,900)
    t_inname= ['Inicial_' date];
    invoke(t_mws,'StoreViewInClipboard')
    invoke(t_mws,'StoreViewInBmpFile', [pwd '\Ey_cloak_off_' t_inname '.bmp'])
ascii_exp(t_treeitem2,t_name_phase,'phase');
ascii_exp(t_treeitem,t_name_mag,'magnitude');
ascii_exp(t_ffitem,t_name_ff,'magnitude');
t_D = importdata(t_name_phase, ' ', 4);
t_E = importdata(t_name_mag, ' ', 4);
t_FF = importdata(t_name_ff, ' ', 4);
xfwc(:,1) = t_D.data(:, 1);       % x-data column
fasewc = t_D.data(:, 2);       % y-data column
ampwc = t_E.data(:, 2);
fasewcwr=unwrap(fasewc,180);
ang_ffn=t_FF.data(:, 1);
mag_ffn=t_FF.data(:, 3);
%% build structure
invoke(t_mws, 'Rebuild');
for i=1:length(xi)
    compname= ['comp' num2str(i)];
    cyl_bld(r1(i)+ks(i)/2,tm+h(i),   ['inner'   num2str(i)],xi(i),dy/2,'Aluminum',compname,h(i),r1(i)-
ks(i)/2,'z');
    cyl_bld(r2(i)+ks(i)/2,tm+h(i),   ['outer'   num2str(i)],xi(i),dy/2,'Aluminum',compname,h(i),r2(i)-
ks(i)/2,'z');
```

```
    invoke(t_group,'AddItem', ['solid$' compname ':inner' num2str(i)],'meshgroup1');
    invoke(t_group,'AddItem', ['solid$' compname ':outer' num2str(i)],'meshgroup1');
    if i<xm
        rot_str(compname,-p, [0 0 0],1,'False','False','ShapeCenter');
    else
        rot_str(compname,p, [0 0 0],1,'False','False','ShapeCenter');
    end
end

%% Run simulation
t_solver = invoke(t_mws, 'Solver');
invoke(t_solver, 'Start');
ascii_exp(t_treeitem,t_name_phase,'phase');
ascii_exp(t_treeitem,t_name_mag,'magnitude');
ascii_exp(t_ffitem,t_name_ff,'magnitude');
t_G = importdata(t_name_phase, ' ', 4);
t_H = importdata(t_name_mag, ' ', 4);
t_FF = importdata(t_name_ff, ' ', 4);
xf(:,1) = t_G.data(:, 1);       % x-data column
fase = t_G.data(:, 2);       % y-data column
amp = t_H.data(:, 2);
fasewr=unwrap(fase,180);
ang_ffi=t_FF.data(:, 1);
mag_ffi=t_FF.data(:, 3);
    invoke(t_mws,'SelectTreeItem','2D/3D Results\E-Field\e-field (f=f)  [gauss_1]\Y')
    invoke(t_mws,'Plot3DPlotsOn2DPlane','True')
    t_cstplot=invoke(t_mws,'ScalarPlot2D');
    invoke(t_cstplot,'PlaneNormal','y')
    invoke(t_cstplot,'PlaneCoordinate',dy/2)
    invoke(t_cstplot,'ScaleToRange','True')
    invoke(t_cstplot,'ScaleRange',-400,400)
    t_inname= ['Inicial_' ];
    invoke(t_mws,'StoreViewInClipboard')
    invoke(t_mws,'StoreViewInBmpFile', [pwd '\Ey_' t_inname '.bmp'])
%% Interpolation with coordinates on the bump's edge
faseb_int=interp1(xfb,faseb,xs(1:xm-1));
fase_int=interp1(xf,fase,xs(1:xm-1));
fasewc_int=interp1(xfwc,fasewc,xs(1:xm-1));
faseb_int2=interp1(xfb,fasebwr,xs(1:xm-1));
fase_int2=interp1(xf,fasewr,xs(1:xm-1));
diff=fase_int-faseb_int;
diff2=fasewc_int-faseb_int;
% Save pictures
    t_picname= ['inicial_phases_' 'Sample_' num2str(num) '.tiff'];
    t_picname2= ['inicial_radii_' 'Sample_' num2str(num) '.tiff'];
    t_picname3= ['inicial_sim_phases_' 'Sample_' num2str(num) '.tiff'];
    t_picname4= ['inicial_diff_phases_' 'Sample_' num2str(num) '.tiff'];
    t_picname5= ['inicial_Farfield_' 'Sample_' num2str(num) '.tiff'];
    t_hplot=figure;
        plot(xi,phis,xi,phitwr);
        saveas(t_hplot,t_picname)
        plot(xi,r1);
        saveas(t_hplot,t_picname2)
        plot(xs(1:xm-1),faseb_int,xs(1:xm-1),fasewc_int,xs(1:xm-1),fase_int)
        saveas(t_hplot,t_picname3)
        bar(xs(1:xm-1), [diff' diff2'])
        saveas(t_hplot,t_picname4)
        plot(ang_ffb,mag_ffb,ang_ffn,mag_ffn,ang_ffi,mag_ffi)
%         axis( [0 180 -100 -60])
        saveas(t_hplot,t_picname5)
        close(t_hplot)

save('inicial_conf','fase_int','fasewc_int','faseb_int','diff','diff2','ang_ffi','mag_ffi','ang_ffb',
'mag_ffb','ang_ffn','mag_ffn')
    % save structure and results
    t_name= ['inicial_sample_param_' date];
    save(t_name, '-regexp', '^(?!t_.*$).')
        phis_cor=phitwr;

%% Interpolation and correction
t_filenamefield= [pwd '\efield.txt'];
r1_cor=r1;
t_fig=figure('Position',  [100, 100, 1049, 748]);
set(t_fig,'CloseRequestFcn',@my_closereq)
while std(diff)>1 || max(abs(diff))>5

    num=num+1;
    t1=tic;
    t_picname= ['corrected_phases_' 'Sample_' num2str(num) '.tiff'];
    t_picname2= ['corr_radii_' 'Sample_' num2str(num) '.tiff'];
    t_picname3= ['corr_sim_phases_' 'Sample_' num2str(num) '.tiff'];
    t_picname4= ['corr_diff_phases_' 'Sample_' num2str(num) '.tiff'];
    t_picname5= ['Farfield_' 'Sample_' num2str(num) '.tiff'];

for i=1:xm-1
            ind_cor(i)=find(par==r1_cor(i));
            if diff(i)>30
                ind_temp=ind_cor(i)+1;
```

```
                ind_temp=mod(ind_temp,length(par));
                if ind_temp==0
                    ind_temp=1;
                end
                ind_cor(i)=ind_temp;
            elseif diff(i)>=5
                    ind_temp=ind_cor(i)+1;
                ind_temp=mod(ind_temp,length(par));
                if ind_temp==0
                    ind_temp=1;
                end
                ind_cor(i)=ind_temp;
%                   phis_cor(i)=phis_cor(i)-diff(i)/10;
            elseif diff(i)<-30
                ind_temp=ind_cor(i)-1;
                ind_temp=mod(ind_temp,length(par));
                if ind_temp==0
                    ind_temp=1;
                end
                ind_cor(i)=ind_temp;
            elseif diff(i)<-5
                ind_temp=ind_cor(i)-1;
                ind_temp=mod(ind_temp,length(par));
                if ind_temp==0
                    ind_temp=1;
                end
                ind_cor(i)=ind_temp;
            end
end

        for ii=1:xm-1
            phis_cor(ii)=phase(ind_cor(ii));
            r1_cor(ii)=par(ind_cor(ii));
            phis_cor(length(xi)-ii+1)=phase(ind_cor(ii));
            r1_cor(length(xi)-ii+1)=par(ind_cor(ii));
        end
        r2_cor=r1_cor+k+w;


           ri(num,:)=r1_cor;
        for i=2:length(ri(:,1))
            if isequal(ri(i-1,:),r1_cor)
                pov=1;
            else
                pov=0;
            end
        end
        if num<=2
            rmse(num)=100*rms(ri(num,:)-r1);
        else
            rmse(num)=100*rms(ri(num,:)-r1);
        end

        if num>10
            per=abs(rmse(num)-rmse(num-2));
            if per==0||pov==1
                display( ['repeated parameter set in ' num2str(num)])
                sendgmail('Repeated parameter set', ['This parameter set num=' num2str(num) ' was
already used, set has been modified'])
                for i=1:xm-1
                    ind_cor(i)=find(par==r1_cor(i));
                    if diff_un(i)>30
                        ind_temp=ind_cor(i)+5;
                        ind_temp=mod(ind_temp,length(par));
                        if ind_temp==0
                            ind_temp=1;
                        end
                        ind_cor(i)=ind_temp;
                    elseif diff_un(i)>=0
                        ind_temp=ind_cor(i)+3;
                        ind_temp=mod(ind_temp,length(par));
                        if ind_temp==0
                            ind_temp=1;
                        end
                        ind_cor(i)=ind_temp;
                        %                       phis_cor(i)=phis_cor(i)-diff(i)/10;
                    elseif diff_un(i)<-30
                        ind_temp=ind_cor(i)-5;
                        ind_temp=mod(ind_temp,length(par));
                        if ind_temp==0
                            ind_temp=1;
                        end
                        ind_cor(i)=ind_temp;
                    elseif diff_un(i)<0
                        ind_temp=ind_cor(i)-3;
                        ind_temp=mod(ind_temp,length(par));
                        if ind_temp==0
                            ind_temp=1;
```

```
                    end
                    ind_cor(i)=ind_temp;
                end
            end

        for ii=1:xm-1
            phis_cor(ii)=phase(ind_cor(ii));
            r1_cor(ii)=par(ind_cor(ii));
            phis_cor(length(xi)-ii+1)=phase(ind_cor(ii));
            r1_cor(length(xi)-ii+1)=par(ind_cor(ii));
        end
         r2_cor=r1_cor+k+w;
            end

        end

        t_hplot=figure;
        plot(xi,phis_cor,xi,phis);
        saveas(t_hplot,t_picname)
        plot(xi,r1_cor,xi,r1);
        saveas(t_hplot,t_picname2)
        close(t_hplot)

        % Update structure
        invoke(t_mws, 'Rebuild');
        for i=1:length(xi)
            compname= ['comp' num2str(i)];
            cyl_bld(r1_cor(i)+ks(i)/2,tm+h(i),                                                    ['inner'
num2str(i)],xi(i),dy/2,'Aluminum',compname,h(i),r1_cor(i)-ks(i)/2,'z');
            cyl_bld(r2_cor(i)+ks(i)/2,tm+h(i),                                                    ['outer'
num2str(i)],xi(i),dy/2,'Aluminum',compname,h(i),r2_cor(i)-ks(i)/2,'z');
            invoke(t_group,'AddItem', ['solid$' compname ':inner' num2str(i)],'meshgroup1');
            invoke(t_group,'AddItem', ['solid$' compname ':outer' num2str(i)],'meshgroup1');
            if i<xm
                rot_str(compname,-p, [0 0 0],1,'False','False','ShapeCenter');
            else
                rot_str(compname,p, [0 0 0],1,'False','False','ShapeCenter');
            end
        end

        % Run simulation
        invoke(t_solver, 'Start');
try
    ascii_exp(t_treeitem2,t_name_phase,'phase');
catch
    disp('error extracting phase, probably simulation stopped abnormally')
     sendgmail('Simulation Error', ['Error extracting phase, probably simulation stopped abnormally at
Sample ' num2str(num) ', skipping set'])
    continue
end
    ascii_exp(t_treeitem,t_name_mag,'magnitude');
    ascii_exp(t_ffitem,t_name_ff,'magnitude');
clear t_G t_H t_I t_FF xf fase amp
    t_G = importdata(t_name_phase, ' ', 4);
    t_H = importdata(t_name_mag, ' ', 4);
    t_FF = importdata(t_name_ff, ' ', 4);
    xf(:,1) = t_G.data(:, 1);       % x-data column
    fase = t_G.data(:, 2);       % y-data column
    amp = t_H.data(:, 2);
    fasewr=unwrap(fase,180);
    clear ang_ff mag_ff
    ang_ff=t_FF.data(:, 1);
    mag_ff=t_FF.data(:, 3);
    diff_ff(num)=20*log10(mag_ffb(1349))-20*log10(mag_ff(1349));
    fase_int=interp1(xf,fase,xs(1:xm-1));
    fase_int2=interp1(xf,fasewr,xs(1:xm-1));
    diff=fase_int-faseb_int;
    diff_un=fase_int2-faseb_int2;
    dev(num)=std(diff);
    rmsea(num)=100*rms(mag_ffb-mag_ff);
    t_hplot=figure;
    plot(xs(1:xm-1),faseb_int,xs(1:xm-1),fasewc_int,xs(1:xm-1),fase_int);
    saveas(t_hplot,t_picname3)
    bar(xs(1:xm-1), [diff' diff2'])
    saveas(t_hplot,t_picname4)
    plot(ang_ff,20*log10(mag_ff),ang_ffb,20*log10(mag_ffb))
    saveas(t_hplot,t_picname5)
    close(t_hplot)
    save(                                                                    ['FF_phase_anal_'
num2str(num)],'fase_int','fasewc_int','faseb_int','diff','diff2','ang_ff','mag_ff')
    % save structure and results
    t_name= ['Sample_' num2str(num)];
    save(t_name, '-regexp', '^(?!t_.*$).')
    vr(num)=toc(t1);
    tot=sum(vr);

        subplot(4,2,1)
        bar( [diff' diff2'])
```

```
        legend('On','Off')
        xlabel('Number of cell')
        ylabel('Phase difference, deg')
        subplot(4,2,2)
        bar(rmsea)
        legend('On','Off')
        xlabel('Number of sample')
        ylabel('RMSE, %')
        subplot(4,2,3)
        bar(rmse)
        title('Radius change')
        xlabel('Number of cell')
        ylabel('RMSE, %')
        subplot(4,2,4)
        bar(diff_ff)
        title('Farfield diff')
        xlabel('Number of sample')
        ylabel('Amplitude difference')
        subplot(4,2,5)
        bar(dev,'b')
        title('Standard deviation')
        xlabel('Number of sample')
        ylabel('Phase difference, deg')
        drawnow;
        subplot(4,2,6)
        plot(ang_ffb,20*log10(mag_ffb),ang_ff,20*log10(mag_ff))
        xlabel('Number of sample')
        title('Farfield')
        ylabel('Amplitude,V/m')
        drawnow;
         subplot(4,2,7)
        bar(vr/60,'r');
        title('Simulation time')
        xlabel('Number of sample')
        ylabel('Time, min')
        subplot(4,2,8)
        barh(tot/3600,'g')
        title('Total time, hour')
        xlabel('Time, hour')

end
```

References

[1] J. Brown, “Artificial dielectrics having refractive indices less than unity,” *Proc. IEE - Part IV Inst. Monogr.*, no. 5, pp. 51 – 62, 1953.

[2] W. Rotman, “Plasma simulation by artificial dielectrics and parallel-plate media,” *IRE Trans. Antennas Propag.*, vol. 10, no. 1, pp. 82–95, Jan. 1962.

[3] R. Marqués, F. Martín, and M. Sorolla, *Metamaterials with negative parameter : theory, design, and microwave applications*. John Wiley & Sons, 2008.

[4] L. Solymar and E. Shamonina, *Waves in Metamaterials*. Oxford University Press, 2009.

[5] J. B. Pendry, “Negative Refraction Makes a Perfect Lens,” *Phys. Rev. Lett.*, vol. 85, no. 18, pp. 3966–3969, Oct. 2000.

[6] V. V. Shevchenko, “The geometric-optics theory of a plane chiral-metamaterial lens,” *J. Commun. Technol. Electron.*, vol. 54, no. 6, pp. 662–666, Jun. 2009.

[7] N. Fang, H. Lee, C. Sun, and X. Zhang, “Sub-diffraction-limited optical imaging with a silver superlens.,” *Science*, vol. 308, no. 5721, pp. 534–7, Apr. 2005.

[8] D. Lu and Z. Liu, “Hyperlenses and metalenses for far-field super-resolution imaging.,” *Nat. Commun.*, vol. 3, p. 1205, 2012.

[9] M. Silveirinha, A. Alù, and N. Engheta, “Parallel-plate metamaterials for cloaking structures,” *Phys. Rev. E*, vol. 75, no. 3, p. 036603, Mar. 2007.

[10] B. Orazbayev, N. Mohammadi Estakhri, M. Beruete, and A. Alù, “Terahertz carpet cloak based on a ring resonator metasurface,” *Phys. Rev. B*, vol. 91, no. 19, p. 195444, 2015.

[11] V. Pacheco-Peña, V. Torres, B. Orazbayev, M. Beruete, M. Navarro-Cía, M. Sorolla Ayza, and N. Engheta, “Mechanical 144 GHz beam steering with all-metallic epsilon-near-zero lens antenna,” *Appl. Phys. Lett.*, vol. 105, no. 24, p. 243503, Dec. 2014.

[12] W. E. Kock, “Metal-Lens Antennas,” *Proc. IRE*, vol. 34, no. 11, pp. 828–836, Nov. 1946.

[13] V. G. Veselago, “The electrodynamics of substances with simultaneously negative values of ε and μ,” *Sov. Phys. Uspekhi*, vol. 10, no. 4, pp. 509–514, Apr. 1968.

[14] J. B. Pendry, a. J. Holden, D. J. Robbins, and W. J. Stewart, “Magnetism from conductors and enhanced nonlinear phenomena,” *IEEE Trans. Microw. Theory Tech.*, vol. 47, no. 11, pp. 2075–2084, 1999.

[15] D. R. Smith, W. J. Padilla, D. C. Vier, S. C. Nemat-Nasser, and S. Schultz, “Composite Medium with Simultaneously Negative Permeability and Permittivity,” *Phys. Rev. Lett.*, vol. 84, no. 18, pp. 4184–4187, May 2000.

[16] D. R. Smith and N. Kroll, “Negative Refractive Index in Left-Handed Materials,” *Phys. Rev. Lett.*, vol. 85, no. 14, pp. 2933–2936, Oct. 2000.

[17] R. A. Shelby, D. R. Smith, and S. Schultz, “Experimental verification of a negative index of refraction.,” *Science*, vol. 292, no. 5514, pp. 77–79, Apr. 2001.

[18] A. Alù, N. Engheta, A. Erentok, and R. W. Ziolkowski, “Electromagnetic Applications Low-index Metamaterials and their Electromagnetic Applications,” vol. 49, no. 1, pp. 23–36, 2007.

[19] A. Sihvola, S. Tretyakov, and A. Baas, “Metamaterials with extreme material parameters,” *J. Commun. Technol. Electron.*, vol. 52, no. 9, pp. 986–990, Sep. 2007.

[20] C. García-Meca, J. Hurtado, J. Martí, A. Martínez, W. Dickson, and A. V. Zayats, “Low-loss multilayered metamaterial exhibiting a negative index of refraction at visible wavelengths,” *Phys. Rev. Lett.*, vol. 106, no. 6, pp. 1–4, 2011.

[21] A. Mary, S. G. Rodrigo, F. J. García-Vidal, and L. Martin-Moreno, “Theory of negative-refractive-index response of double-fishnet structures,” *Phys. Rev. Lett.*, vol. 101, no. 10, p. 103902, Sep. 2008.

[22] M. Beruete, M. Navarro-Cía, M. Sorolla Ayza, and I. Campillo, “Negative refraction through an extraordinary transmission left-handed metamaterial slab,” *Phys. Rev. B*, vol. 79, no. 19, p. 195107, May 2009.

[23] M. Beruete, M. Sorolla Ayza, and I. Campillo, “Left-handed extraordinary optical transmission through a photonic crystal of subwavelength hole arrays,” *Opt. Express*, vol. 14, no. 12, p. 5445, 2006.

[24] T. W. Ebbesen, H. J. Lezec, H. F. Ghaemi, T. Thio, and P. A. Wolff, “Extraordinary optical transmission through sub-wavelength hole arrays,” vol. 391, no. 6668, pp. 667–669, Feb. 1998.

[25] M. Beruete, M. Sorolla Ayza, I. Campillo, J. S. Dolado, L. Martín-Moreno, J. Bravo-Abad, and F. J. García-Vidal, “Enhanced millimeter-wave transmission through subwavelength hole arrays.,” *Opt. Lett.*, vol. 29, no. 21, pp. 2500–2, Nov. 2004.

[26] G. Dolling, C. Enkrich, M. Wegener, C. M. Soukoulis, and S. Linden, “Simultaneous negative phase and group velocity of light in a metamaterial.,” *Science*, vol. 312, no. 5775, pp. 892–4, May 2006.

[27] M. Navarro-Cía, M. Beruete, M. Sorolla, I. Campillo, M. Sorolla Ayza, and I. Campillo, “Negative refraction in a prism made of stacked subwavelength hole arrays.,” *Opt. Express*, vol. 16, no. 2, pp. 560–566, Jan. 2008.

[28] S. Zhang, W. Fan, N. Panoiu, K. Malloy, R. Osgood, and S. Brueck, “Experimental Demonstration of Near-Infrared Negative-Index Metamaterials,” *Phys. Rev. Lett.*, vol. 95, no. 13, p. 137404, Sep. 2005.

[29] M. Beruete, M. Sorolla, I. Campillo, and J. S. Dolado, “Increase of the transmission in cut-off metallic hole arrays,” *IEEE Microw. Wirel. Components Lett.*, vol. 15, no. 2, pp. 116–118, Feb. 2005.

[30] L. Martin-Moreno, F. J. García-Vidal, H. J. Lezec, K. M. Pellerin, T. Thio, J. B. Pendry, and T. W. Ebbesen, “Theory of extraordinary optical transmission through subwavelength hole arrays,” *Nature*, vol. 86, p. 4, 2000.

[31] R. S. Penciu, M. Kafesaki, T. Koschny, E. N. Economou, and C. M. Soukoulis, “Magnetic response of nanoscale left-handed metamaterials,” *Phys. Rev. B*, vol. 81, no. 23, p. 235111, Jun. 2010.

[32] M. Beruete, M. Navarro-Cía, M. Sorolla Ayza, and I. Campillo, “Planoconcave lens by negative refraction of stacked subwavelength hole arrays,” *Opt. Express*, vol. 16, no. 13, pp. 9677–9683, Jun. 2008.

[33] M. Navarro-Cía, M. Beruete, M. Sorolla Ayza, I. Campillo, M. Sorolla, I. Campillo, M. Sorolla Ayza, and I. Campillo, “Converging biconcave metallic lens by double-negative extraordinary transmission metamaterial,” *Appl. Phys. Lett.*, vol. 94, no. 14, p. 144107, Apr. 2009.

[34] M. Navarro-Cía, M. Beruete, I. Campillo, and M. Sorolla Ayza, “Beamforming by Left-Handed Extraordinary Transmission Metamaterial Bi- and Plano-Concave Lens at Millimeter-Waves,” *IEEE Trans. Antennas Propag.*, vol. 59, no. 6, pp. 2141–2151, Jun. 2011.

[35] V. Pacheco-Peña, B. Orazbayev, V. Torres, M. Beruete, and M. Navarro-Cía, “Ultra-compact planoconcave zoned metallic lens based on the fishnet metamaterial,” *Appl. Phys. Lett.*, vol. 103, pp. 183507–1–12, 2013.

[36] V. Pacheco-Peña, B. Orazbayev, U. Beaskoetxea, M. Beruete, and M. Navarro-Cía, “Zoned Near-Zero Refractive Index Fishnet Lens Antenna : Steering Millimeter Waves,” *J. Appl. Phys.*, vol. 115, pp. 124902–1–8, 2014.

[37] B. Orazbayev, V. Pacheco-Peña, M. Beruete, and M. Navarro-Cía, “Exploiting the dispersion of the double-negative-index fishnet metamaterial to create a broadband low-profile metallic lens,” *Opt. Express*, vol. 23, no. 7, p. 8555, Mar. 2015.

[38] B. Orazbayev, M. Beruete, V. Pacheco-Peña, G. Crespo, J. Teniente, and M. Navarro-Cía, “Soret fishnet metalens antenna.,” *Sci. Rep.*, vol. 4, p. 9988, Jan. 2015.

[39] N. Yu, P. Genevet, M. a Kats, F. Aieta, J.-P. Tetienne, F. Capasso, and Z. Gaburro, “Light propagation with phase discontinuities: generalized laws of reflection and refraction.,” *Science*, vol. 334, no. 6054, pp. 333–7, Oct. 2011.

[40] X. Ni, N. K. Emani, A. V Kildishev, A. Boltasseva, and V. M. Shalaev, “Broadband light bending with plasmonic nanoantennas.,” *Science*, vol. 335, no. 6067, p. 427, Jan. 2012.

[41] L. Huang, X. Chen, H. Mühlenbernd, G. Li, B. Bai, Q. Tan, G. Jin, T. Zentgraf, and S. Zhang, “Dispersionless phase discontinuities for controlling light propagation,” *Nano Lett.*, vol. 12, no. 11, pp. 5750–5755, 2012.

[42] F. Aieta, P. Genevet, M. a. Kats, N. Yu, R. Blanchard, Z. Gaburro, and F. Capasso, “Aberration-free ultrathin flat lenses and axicons at telecom wavelengths based on plasmonic metasurfaces,” *Nano Lett.*, vol. 12, no. 9, pp. 4932–4936, 2012.

[43] X. Chen, L. Huang, H. Mühlenbernd, G. Li, B. Bai, Q. Tan, G. Jin, C.-W. Qiu, S. Zhang, and T. Zentgraf, “Dual-polarity plasmonic metalens for visible light.,” *Nat. Commun.*, vol. 3, p. 1198, Jan. 2012.

[44] N. Yu, F. Aieta, P. Genevet, M. a. Kats, Z. Gaburro, and F. Capasso, "A broadband, background-free quarter-wave plate based on plasmonic metasurfaces," *Nano Lett.*, vol. 12, no. 12, pp. 6328–6333, 2012.

[45] U. Leonhardt, "Optical conformal mapping.," *Science*, vol. 312, no. 5781, pp. 1777–80, Jun. 2006.

[46] J. B. Pendry, D. Schurig, and D. R. Smith, "Controlling electromagnetic fields.," *Science*, vol. 312, no. 5, pp. 1780–1782, Jun. 2006.

[47] A. Alù and N. Engheta, "Achieving transparency with plasmonic and metamaterial coatings," *Phys. Rev. E*, vol. 72, no. 1, p. 016623, Jul. 2005.

[48] D. Rainwater, a. Kerkhoff, K. Melin, J. C. Soric, G. Moreno, and A. Alù, "Experimental verification of three-dimensional plasmonic cloaking in free-space," *New J. Phys.*, vol. 14, 2012.

[49] C. Huygens, *Traite de la lumiere*. Leiden, 1690.

[50] H. D. Hristov, *Fresnel Zones in Wireless Links, Zone Plate Lenses and Antennas*. Artech House, Norwood, MA, 2000.

[51] I. V Minin and O. Minin, *Diffractional Optics of Millimetre Waves*. CRC Press, Bristol, 2004.

[52] T. Weiland, "A discretization method for the solution of Maxwell's equations for six-component Field," *Int. J. Electron. Commun.*, vol. 31, no. 3, pp. 116–120, 1977.

[53] CST Computer Simulation Technology AG, "CST Microwave Studio." http://www.cst.com, 2015.

[54] "AB Millimetre." [Online]. Available: http://www.abmillimetre.com/.

[55] P. F. Goldsmith, "Zone plate lens antennas for millimeter and submillimeter wavelengths," in *The Third International Symposium on Space Terahertz Technology: Symposium Proceedings*, 1992, pp. 345–361.

[56] X. Chen, T. Grzegorczyk, B.-I. Wu, J. Pacheco, and J. Kong, "Robust method to retrieve the constitutive effective parameters of metamaterials," *Phys. Rev. E*, vol. 70, no. 1, p. 016608, Jul. 2004.

[57] M. Navarro-Cía, M. Beruete, I. Campillo, and M. Sorolla, "Enhanced lens by ε and μ near-zero metamaterial boosted by extraordinary optical transmission," *Phys. Rev. B - Condens. Matter Mater. Phys.*, vol. 83, no. 11, pp. 115112–1–5, Mar. 2011.

[58] D. F. Filipovic and G. M. Rebeiz, "Double-slot antennas on extended hemispherical and elliptical quartz dielectric lenses," *Int. J. Infrared Millimeter Waves*, vol. 14, no. 10, pp. 1905–1924, Oct. 1993.

[59] N. Llombart, G. Chattopadhyay, A. Skalare, and I. Mehdi, "Novel Terahertz Antenna Based on a Silicon Lens Fed by a Leaky Wave Enhanced Waveguide," *IEEE Trans. Antennas Propag.*, vol. 59, no. 6, pp. 2160–2168, Jun. 2011.

[60] D. L. Runyon, “Optimum directivity coverage of fan-beam antennas,” *IEEE Antennas Propag. Mag.*, vol. 44, no. 2, pp. 66–70, Apr. 2002.

[61] J. L. Soret, “Ueber die durch Kreisgitter erzeugten Diffractionsphänomene,” *Ann. der Phys. und Chemie*, vol. 232, no. 9, pp. 99–113, 1875.

[62] H. Hristov and M. Herben, “Millimeter-wave Fresnel-zone plate lens and antenna,” *IEEE Trans. Microw. Theory Tech.*, vol. 43, no. 12, pp. 2779–2785, 1995.

[63] T. Matsui, A. Agrawal, A. Nahata, and Z. V. Vardeny, “Transmission resonances through aperiodic arrays of subwavelength apertures.,” *Nature*, vol. 446, no. 7135, pp. 517–21, Mar. 2007.

[64] S. Enoch, G. Tayeb, P. Sabouroux, N. Guérin, and P. Vincent, “A Metamaterial for Directive Emission,” *Phys. Rev. Lett.*, vol. 89, no. 21, p. 213902, Nov. 2002.

[65] A. Alù, M. M. Silveirinha, A. Salandrino, and N. Engheta, “Epsilon-near-zero metamaterials and electromagnetic sources: Tailoring the radiation phase pattern,” *Phys. Rev. B*, vol. 75, no. 15, p. 155410, Apr. 2007.

[66] R. Ziolkowski, “Propagation in and scattering from a matched metamaterial having a zero index of refraction,” *Phys. Rev. E*, vol. 70, no. 4, p. 046608, Oct. 2004.

[67] M. Beruete, I. Campillo, J. S. Dolado, J. E. Rodriguez-Seco, E. Perea, F. Falcone, and M. Sorolla Ayza, “Very Low-Profile ‘Bull’s Eye’ Feeder Antenna,” *Antennas Wirel. Propag. Lett.*, vol. 4, no. 1, pp. 365–368, 2005.

[68] M. Beruete, M. Navarro-Cía, F. Falcone, M. Sorolla, I. Campillo, J. E. Rodriguez-Seco, E. Perea, and I. J. Nunez-Manrique, “Extraordinary Transmission surfaces as superstrate,” in *2009 Mediterrannean Microwave Symposium (MMS)*, 2009, pp. 1–4.

[69] G. a. Hurd, *IEEE Standard Test Procedures for Antennas*, vol. 26, no. 79. 1980.

[70] N. Engheta and R. W. Ziolkowski, *Metamaterials: Physics and Engineering Explorations*. Hoboken, NJ, USA: John Wiley & Sons, Inc., 2006.

[71] D. Schurig, J. J. Mock, B. J. Justice, S. A. Cummer, J. B. Pendry, A. F. Starr, and D. R. Smith, “Metamaterial electromagnetic cloak at microwave frequencies.,” *Science*, vol. 314, no. 2003, pp. 977–980, 2006.

[72] D. Shin, Y. Urzhumov, Y. Jung, G. Kang, S. Baek, M. Choi, H. Park, K. Kim, and D. R. Smith, “Broadband electromagnetic cloaking with smart metamaterials.,” *Nat. Commun.*, vol. 3, p. 1213, Jan. 2012.

[73] N. Landy and D. R. Smith, “A full-parameter unidirectional metamaterial cloak for microwaves.,” *Nat. Mater.*, vol. 12, no. 1, pp. 25–8, Jan. 2013.

[74] A. Alù, M. Silveirinha, and N. Engheta, “Transmission-line analysis of ε-near-zero–filled narrow channels,” *Phys. Rev. E*, vol. 78, no. 1, p. 016604, Jul. 2008.

[75] A. Alù and N. Engheta, “Plasmonic materials in transparency and cloaking problems: mechanism, robustness, and physical insights.,” *Opt. Express*, vol. 15, no. 6, pp. 3318–3332, 2007.

[76] F. Monticone and A. Alù, “Do cloaked objects really scatter less?,” *Phys. Rev. X*, vol. 3, no. 4, p. 041005, Oct. 2014.

[77] J. Li and J. B. Pendry, “Hiding under the Carpet: A New Strategy for Cloaking,” *Phys. Rev. Lett.*, vol. 101, no. 20, p. 203901, Nov. 2008.

[78] R. Liu, C. Ji, J. J. Mock, J. Y. Chin, T. J. Cui, and D. R. Smith, “Broadband ground-plane cloak.,” *Science*, vol. 323, no. January, pp. 366–369, 2009.

[79] P. Zhang, M. Lobet, and S. He, “Carpet cloaking on a dielectric half-space.,” *Opt. Express*, vol. 18, no. 17, pp. 18158–63, Aug. 2010.

[80] B. Zhang, T. Chan, and B. I. Wu, “Lateral shift makes a ground-plane cloak detectable,” *Phys. Rev. Lett.*, vol. 104, no. June, pp. 1–4, 2010.

[81] J. Zhang, Z. Lei Mei, W. Ru Zhang, F. Yang, and T. Jun Cui, “An ultrathin directional carpet cloak based on generalized Snell’s law,” *Appl. Phys. Lett.*, vol. 103, no. 15, p. 151115, 2013.

[82] N. M. Estakhri and A. Alù, “Ultra-Thin Unidirectional Carpet Cloak and Wavefront Reconstruction With Graded Metasurfaces,” *IEEE Antennas Wirel. Propag. Lett.*, vol. 13, no. c, pp. 1775–1778, 2014.

[83] N. Mohammadi Estakhri, C. Argyropoulos, and A. Alù, “Graded Metascreens to Enable a New Degree of Nanoscale Light Management,” *Philos. Trans. R. Soc. London*, 2015.

[84] D. L. Sounas and A. Alù, “Extinction symmetry for reciprocal objects and its implications on cloaking and scattering manipulation,” *Opt. Lett.*, vol. 39, no. 13, p. 4053, 2014.

[85] I. Moreno and C.-C. Sun, “Modeling the radiation pattern of LEDs,” *Opt. Express*, vol. 16, no. 3, p. 1808, 2008.

[86] C. Daniel and F. S. Wood, *Fitting Equations to Data: Computer Analysis of Multifactor Data for Scientists and Engineers*. New York: John Wiley & Sons Canada, 1971.

7 Author's merits

Journal papers

1. B. Orazbayev, N. Mohammadi Estakhri, M. Beruete, and A. Alù, "Terahertz carpet cloak based on a ring resonator metasurface," Phys. Rev. B, vol. 91, no. 19, p. 195444, 2015.
2. B. Orazbayev, M. Beruete, V. Pacheco-Peña, G. Crespo, J. Teniente, and M. Navarro-Cía, "Soret fishnet metalens antenna.," Sci. Rep., vol. 4, p. 9988, Jan. 2015.
3. B. Orazbayev, V. Pacheco-Peña, M. Beruete, and M. Navarro-Cía, "Exploiting the dispersion of the double-negative-index fishnet metamaterial to create a broadband low-profile metallic lens," Opt. Express, vol. 23, no. 7, p. 8555, Mar. 2015.
4. V. Pacheco-Peña, M. Navarro-Cia, B. Orazbayev, I. Minin, O. Minin, and M. Beruete, "Zoned Fishnet Lens Antenna with Reference Phase for Side Lobe Reduction," IEEE Trans. Antennas Propag., vol. PP, no. 99, pp. 1–1, 2015.
5. V. Torres, B. Orazbayev, V. Pacheco-Peña, J. Teniente, M. Beruete, M. Navarro-Cía, M. S. Ayza, and N. Engheta, "Experimental Demonstration of a Millimeter-Wave Metallic ENZ Lens Based on the Energy Squeezing Principle," IEEE Trans. Antennas Propag., vol. 63, no. 1, pp. 231–239, 2015.
6. U. Beaskoetxea, V. Pacheco-Peña, B. Orazbayev, T. Akalin, S. Maci, M. Navarro-Cía, and M. Beruete, "77 GHz High Gain Bull's-Eye Antenna With Sinusoidal Profile," IEEE Antennas Wirel. Propag. Lett., vol. PP, no. 99, pp. 1–1, 2014.
7. V. Pacheco-Peña, V. Torres, B. Orazbayev, M. Beruete, M. Navarro-Cía, M. Sorolla Ayza, and N. Engheta, "Mechanical 144 GHz beam steering with all-metallic epsilon-near-zero lens antenna," Appl. Phys. Lett., vol. 105, no. 24, p. 243503, Dec. 2014.
8. V. Pacheco-Peña, B. Orazbayev, U. Beaskoetxea, M. Beruete, and M. Navarro-Cía, "Zoned Near-Zero Refractive Index Fishnet Lens Antenna : Steering Millimeter Waves," J. Appl. Phys., vol. 115, pp. 124902–1–8, 2014.
9. V. Pacheco-Peña, B. Orazbayev, V. Torres, M. Beruete, and M. Navarro-Cía, "Ultra-compact planoconcave zoned metallic lens based on the fishnet metamaterial," Appl. Phys. Lett., vol. 103, pp. 183507–1–12, 2013.

International Conferences

1. V. Torres, B. Orazbayev, V. Pacheco-Peña, J. Teniente, M. Beruete, Miguel Navarro- Cía, Mario Sorolla Ayza, Nader Engheta, "144 GHz Epsilon-Near-Zero Metamaterial Lens", The 9th European Conference on Antennas and Propagation (EuCAP 2015), (2015)
2. B. Orazbayev, V. Pacheco-Peña, V. Torres, M. Beruete, M. Navarro-Cía, "Zoned fishnet metamaterial lens with millimetre wave dual-band response", The 9th European Conference on Antennas and Propagation (EuCAP 2015), (2015)
3. U. Beaskoetxea, V. Pacheco-Peña, B. Orazbayev, T. Akalin, S. Maci, M. Navarro-Cía, M. Beruete, "High Gain Flat 77GHz Sinusoidal Bull's Eye", The 9th European Conference on Antennas and Propagation (EuCAP 2015), (2015)
4. V. Pacheco-Peña, B. Orazbayev, P. Rodríguez-Ulibarri, M. Beruete, M. Navarro-Cía, "Focusing Millimeter Waves Using a Zoned Fishnet Metalens ", 14th Mediterranean Microwave Symposium, MMS 2014, (2014)
5. B. Orazbayev, V. Torres, V. Pacheco-Peña, P. Rodríguez-Ulibarri, J. Teniente, M. Beruete, M. Sorolla, M. Navarro-Cía, N. Engheta, "All-Metallic ε-Near-Zero (ENZ) Lens Based On Ultra-Narrow Hollow Rectangular Waveguides: Experimental Results", 14th Mediterranean Microwave Symposium, MMS 2014, (2014)
6. V. Pacheco-Peña, V. Torres, B. Orazbayev, M. Beruete, M. Navarro-Cía, N. Engheta, "Focusing Millimetre Waves by Means of a Permittivity-Near Zero Narrow-Waveguide Lens", 8th International Congress on Advanced Electromagnetic Materials in Microwaves and Optics, Metamaterials 2014, (2014)
7. V. Pacheco-Peña, B. Orazbayev, U. Beaskoetxea, V. Torres, M. Beruete, M. Navarro-Cía, "All-metallic Zoned Fishnet Metamaterial Lens for the Unlicensed Millimetre-wave V-band", 8th International Congress on Advanced Electromagnetic Materials in Microwaves and Optics, Metamaterials 2014, (2014)
8. M. Sorolla, M. Beruete, F. Falcone, V. Torres, V. Pacheco-Peña, B. Orazbayev, P. Rodríguez-Ulibarri, M. Navarro-Cía, "From the Extraordinary Transmission to the Zoned Fishnet Metamaterial Lens", 2014 IEEE International Symposium on Antennas and Propagation and USNC-URSI National Radio Science Meeting, (2014)
9. V. Pacheco-Peña, B. Orazbayev, V. Torres, M. Beruete, M. Navarro-Cía, "Slimming the Fishnet Metamaterial Lens", 8th European Conference on Antennas and Propagation, EuCAP 2014, (2014)
10. B. Orazbayev, V. Torres, V. Pacheco-Peña, P. Rodríguez-Ulibarri, J. Teniente, M. Beruete, M. Navarro-Cía, N. Engheta, "All-Metallic ε-Near-Zero (ENZ) Lens Based On Ultra-Narrow Hollow Rectangular Waveguides: Experimental Results", 14th Mediterranean Microwave Symposium (MMS), (2014)
11. P. Rodríguez-Ulibarri, B. Orazbayev, V. Torres, M. Beruete, M. Navarro-Cía, " Controlling Extraordinary Transmission By Means Of Hedgehog Subwavelength Hole Arrays", Metamaterials 2013 , (2013)

National Conferences

1. V. Pacheco-Peña, V. Torres, B. Orazbayev, M. Beruete, M. Navarro-Cía, N. Engheta, "Plano-concave lens based on ultra-narrow hollow rectangular waveguides mimicking an effective ENZ medium", XXIX Simposium Nacional de la Unión Científica Internacional de Radio, (2014)
2. B. Orazbayev, V. Pacheco-Peña, V. Torres, M. Beruete, M. Navarro-Cía, "Zoning technique application for the fishnet metamaterial lens", XXIX Simposium Nacional de la Unión Científica Internacional de Radio, (2014)
3. V. Torres, B. Orazbayev, P. Rodríguez-Ulibarri, M. Beruete, M. Navarro-Cía, "Control de la Transmisión Extraordinaria mediante pines metálicos ortogonales al Plano de los Agujeros Sublambda", XXVIII Simposium Nacional de la Unión Científica Internacional de Radio, URSI 2013, (2013)